Communications on Applied Mathematics and Computation
https://doi.org/10.1007/s42967-021-00153-2

ORIGINAL PAPER

A New Hybrid WENO Scheme with the High-Frequency Region for Hyperbolic Conservation Laws

Yifei Wan[1] · **Yinhua Xia**[1]

Received: 11 February 2021 / Revised: 1 June 2021 / Accepted: 2 July 2021
© Shanghai University 2021

Abstract

In this paper, a new kind of hybrid method based on the weighted essentially non-oscillatory (WENO) type reconstruction is proposed to solve hyperbolic conservation laws. Comparing the WENO schemes with/without hybridization, the hybrid one can resolve more details in the region containing multi-scale structures and achieve higher resolution in the smooth region; meanwhile, the essentially oscillation-free solution could also be obtained. By adapting the original smoothness indicator in the WENO reconstruction, the stencil is distinguished into three types: smooth, non-smooth, and high-frequency region. In the smooth region, the linear reconstruction is used and the non-smooth region with the WENO reconstruction. In the high-frequency region, the mixed scheme of the linear and WENO schemes is adopted with the smoothness amplification factor, which could capture high-frequency wave efficiently. Spectral analysis and numerous examples are presented to demonstrate the robustness and performance of the hybrid scheme for hyperbolic conservation laws.

Keywords Hybrid schemes · WENO reconstruction · Smoothness indicator · Finite difference method

Mathematics Subject Classification 65M06 · 35L65

Yinhua Xia: Research supported by the National Numerical Windtunnel Project NNW2019ZT4-B08 and the NSFC grant No. 11871449.

✉ Yinhua Xia
yhxia@ustc.edu.cn

Yifei Wan
wanyifei@mail.ustc.edu.cn

[1] School of Mathematical Sciences, University of Science and Technology of China, Hefei 230026, Anhui, China

Published online: 24 November 2021

1 Introduction

The hyperbolic conservation laws take a great part in numerical simulations. To solve complex flow field, we need a high resolution scheme to resolve the small scales, and compress numerical oscillations. In 1987, Harten et al. [17] proposed the essentially non-oscillatory (ENO) scheme to solve problems for one-dimensional hyperbolic conservation law, in which the key idea was to identify the smoothest stencil for reconstruction based on the divided difference. In 1994, Liu et al. [27] designed the original weighted essentially non-oscillatory (WENO) scheme which used the convex combination of the sub-stencils and the nonlinear weights to recover its corresponding linear weights in smooth region and compressed the weight of the stencil containing shock nearly zero, and thus achieved the ENO property. To improve accuracy, Jiang and Shu [19] proposed a new smoothness indicator which is widely used in lots of WENO schemes. The original WENO scheme equipped with this smoothness indicator is named as the WENOJS scheme. Since the WENOJS scheme may lose accuracy in critical points, to overcome this defect, Henrick et al. [18] proposed the WENO-M scheme which used mapping to modify the nonlinear weight, but this strategy increased about 20% CPU time. Borges et al. [5] proposed the WENOZ scheme which can give the numerical solution with low dissipation, while the computational cost is almost the same as the WENOJS scheme, and there is a parameter in the scheme that can be tuned to recover accuracy near critical points and to adjust dissipation. Afterward, lots of new smoothness indicators were designed [3, 4, 10, 15, 20, 42–44] to improve the performance of WENO-type schemes. People also proposed lots of hybrid WENO schemes to improve the performance, such as hybrid compact-ENO schemes [2], conservative hybrid compact-WENO schemes [29], characteristic-wise hybrid compact-WENO schemes [32], multi-domain hybrid spectral-WENO methods [8]. The a posteriori, efficient, high-spectral resolution hybrid finite difference method [11], hybrid compact-WENO finite difference schemes with shock detectors based on the conjugate Fourier algorithm [9], radial basis function [39], and artificial neural network [40], etc.

It has been pointed out by Acker et al. in [1] that increasing the weight of non-smooth stencil is of great importance to give better resolution on coarse grid, while increasing the accuracy near critical points works on fine grid. In view of this point, we design a new kind of hybrid scheme to improve the existing WENO schemes, which can give the numerical solution with lower dissipation and less error in smooth region and suppress numerical oscillation effectively. For general hybrid methods [23–25, 45, 46], people often classify the whole domain into two parts: smooth region and non-smooth region, and use the corresponding linear scheme in smooth region while certain WENO scheme in non-smooth region. The effect of these hybrid methods is heavily based on the proposed shock detector, such as the discontinuity indicator based on the average total variation of the solution [31, 47], the minmod-based TVB limiter [7], Harten's multi-resolution analysis [16], the shock detection technique by Krivodonova et al. [21], the trigonometric detector-based conjugate Fourier analysis [9], the shock detection method based on radial basis function [39], the monotonicity-preserving discontinuity indicator [38], the shock detection method based on targeted ENO schemes [12, 13], and the shock detection method based on neural network [37, 40], etc. Different from the general approach in the hybrid schemes, we classify the whole domain into three parts: smooth, non-smooth, and high-frequency regions.

In this paper, we propose a very simple shock detector to distinguish the smooth region from the whole domain, which is based on the smoothness indicator in the WENO reconstruction and similar to the approach in [4] for the third-order WENO scheme. The issue for recovering accuracy near critical points is also a hot topic for WENO schemes. There is a strategy to deal with it by setting the small quantity arising in the nonlinear weight as a mesh size-dependent quantity, which appears in numerous literatures [1, 6, 42, 43]. We develop an alternative simple strategy to achieve the same goal by enforcing a threshold to include critical points in the smooth region. The rest domain is further identified as the non-smooth or high-frequency region with a detector also based on the smoothness indicator in the WENO reconstruction. As usual, the linear reconstruction and the WENO reconstruction are used in the smooth and non-smooth regions, respectively. In high-frequency region, a mixed scheme of the linear and WENO reconstruction is developed to improve the resolution on high-frequency waves, which is verified by the numerical spectral analysis. Compared with the WENO scheme without hybridization, this strategy can obtain numerical solutions with higher resolution and maintain the good capture of the outline near discontinuities.

Among all the high-order WENO schemes, the fifth-order WENO scheme is the most popular one, since this scheme maintains sufficiently low dissipation to capture shock, while some oscillation may appear for higher order WENO schemes due to the usage of larger sub-stencil. We apply our hybrid strategy to the fifth-order WENOJS and WENOZ finite difference schemes, respectively, named as WENOJS-H and WENOZ-H schemes. Detailed comparisons with the original and the hybrid schemes are presented, which demonstrate that the hybrid schemes could give slightly sharper approximation near the discontinuities, and yield better results especially in the sophisticated region containing many small scales at slightly smaller computational cost. From spectral analysis [29] and numerical experiments, we can also see that these hybrid schemes work quite similarly. To some extent, the hybrid strategy can exploit the potential of the original scheme sufficiently.

The rest of the paper is organized as follows. In Sect. 2, we briefly introduce the WENO finite difference method for hyperbolic conservation laws, including the WENOJS and WENOZ reconstruction. Section 3 is devoted to the development of the hybrid strategy. First, we propose a simple detector to distinguish three different regions, which is also based on the smoothness indicator in the WENO reconstruction. Also, a mixed reconstruction in the high-frequency region is developed. The approximate spectral analysis is performed to show the improvement of the hybrid schemes on the dispersion and dissipation relations. In Sect. 4, numerous experiment results are presented to show the robustness and high resolution feature of these new hybrid WENO schemes. Conclusions and perspectives are drawn in Sect. 5.

2 The WENO Finite Difference Method

In this section, we will briefly introduce the finite difference method with the sliding operator and the WENO reconstruction.

2.1 The Conservative Finite Difference Method

For the one-dimensional scalar conservation law

$$u_t + f(u)_x = 0, x \in [a, b], \tag{1}$$

we solve it on a uniform grid, $a = x_{\frac{1}{2}} < x_{\frac{3}{2}} < \cdots < x_{N+\frac{1}{2}} = b$. Define $I_i = [x_{i-\frac{1}{2}}, x_{i+\frac{1}{2}}]$, $\Delta x = x_{i+\frac{1}{2}} - x_{i-\frac{1}{2}}$ and x_i are the centers of the cells I_i, for $i = 1, 2, \cdots, N$. Let $h(x)$ be the sliding function satisfying

$$\frac{\int_{x-\frac{\Delta x}{2}}^{x+\frac{\Delta x}{2}} h(\xi)\mathrm{d}\xi}{\Delta x} = f(u(x,t)). \tag{2}$$

Then

$$f(u)_x = \frac{h\left(x + \frac{\Delta x}{2}\right) - h\left(x - \frac{\Delta x}{2}\right)}{\Delta x}. \tag{3}$$

Thus, Eq. (1) can be discretized in conservative form

$$\frac{\mathrm{d}u_i}{\mathrm{d}t} = -\frac{\hat{f}_{i+\frac{1}{2}} - \hat{f}_{i-\frac{1}{2}}}{\Delta x}, \tag{4}$$

where u_i is the numerical approximation to the point value $u(x_i, t)$, and the numerical flux $\hat{f}_{i+\frac{1}{2}}$ is the approximation of $h(x_{i+\frac{1}{2}}, t)$ obtained by reconstruction. In the reconstruction, $f(u_i)$ can be viewed as the approximation of the cell average of the sliding function $\bar{h}_i = \frac{1}{\Delta x}\int_{x_{i+\frac{1}{2}}}^{x_{i-\frac{1}{2}}} h(x)\mathrm{d}x$. Therefore, we need to reconstruct $\hat{f}_{i+\frac{1}{2}} = h_{i+\frac{1}{2}}$ from the cell average $\bar{h}_i$. To maintain stability, the upwind mechanism is performed by the flux splitting, e.g., the Lax-Friedrichs splitting $\hat{f}_{i+\frac{1}{2}} = \hat{f}^+_{i+\frac{1}{2}} + \hat{f}^-_{i+\frac{1}{2}}$ with $f^{\pm}(u) = \frac{1}{2}(f(u) \pm \alpha u)$ and $\alpha = \max_u |f'(u)|$ chosen in the relevant domain.

Similarly, the one-dimensional hyperbolic system

$$\boldsymbol{u}_t + \boldsymbol{f}(\boldsymbol{u})_x = \boldsymbol{0}, x \in [a,b] \tag{5}$$

can be discretized as

$$\frac{\mathrm{d}\boldsymbol{u}_i}{\mathrm{d}t} = -\frac{\hat{\boldsymbol{f}}_{i+\frac{1}{2}} - \hat{\boldsymbol{f}}_{i-\frac{1}{2}}}{\Delta x}, \tag{6}$$

where $\boldsymbol{u}_i$ is the approximation to $\boldsymbol{u}(x_i, t)$. The easiest way is to reconstruct $\hat{\boldsymbol{f}}_{i+\frac{1}{2}}$ in a component-wise fashion. However, for more demanding problems or when the order of accuracy is high, the more robust characteristic decomposition is needed. Let $\boldsymbol{R} = \boldsymbol{R}(\boldsymbol{u}_{i+\frac{1}{2}}), \boldsymbol{L} = \boldsymbol{R}^{-1}(\boldsymbol{u}_{i+\frac{1}{2}}), \boldsymbol{\Lambda} = \boldsymbol{\Lambda}(\boldsymbol{u}_{i+\frac{1}{2}})$ be the matrices of right eigenvectors, left eigenvectors, and eigenvalues of the Jacobian $\boldsymbol{f}'(\boldsymbol{u}_{i+\frac{1}{2}})$, respectively. The average state $\boldsymbol{u}_{i+\frac{1}{2}}$ computed by a Roe average satisfies

$$\boldsymbol{f}(\boldsymbol{u}_{i+1}) - \boldsymbol{f}(\boldsymbol{u}_i) = \boldsymbol{f}'(\boldsymbol{u}_{i+\frac{1}{2}})(\boldsymbol{u}_{i+1} - \boldsymbol{u}_i). \tag{7}$$

Transform the point value $\boldsymbol{u}_j$ and $\boldsymbol{f}(\boldsymbol{u}_j)$ into local characteristic field by

$$\boldsymbol{v}_j = \boldsymbol{L}\boldsymbol{u}_j, \boldsymbol{g}_j = \boldsymbol{L}\boldsymbol{f}_j, j = i-2, \cdots, i+3. \tag{8}$$

Next, we perform the Lax-Friedrichs flux splitting for each characteristic variable and the WENO reconstruction to obtain the corresponding component of the flux $\hat{\boldsymbol{g}}^{\pm}_{i+\frac{1}{2}}$. The viscosity coefficient in the Lax-Friedrichs flux splitting can be taken as $\alpha_l = \max_j |\lambda_l(\boldsymbol{u}_j)|$ for each characteristic variable in the relevant domain. Then, we project the new flux $\hat{\boldsymbol{g}}^{\pm}_{i+\frac{1}{2}}$ back into physical space by

$$\hat{\boldsymbol{f}}^{\pm}_{i+\frac{1}{2}} = \boldsymbol{R}\hat{\boldsymbol{g}}^{\pm}_{i+\frac{1}{2}}. \tag{9}$$

The final numerical flux is formed by $\hat{\boldsymbol{f}}_{i+\frac{1}{2}} = \hat{\boldsymbol{f}}^{+}_{i+\frac{1}{2}} + \hat{\boldsymbol{f}}^{-}_{i+\frac{1}{2}}$.

For multi-dimensional hyperbolic conservation laws on uniform grids, the similar procedure can be performed in a dimension-by-dimension way to obtain the corresponding finite difference scheme in conservative form. We refer to [35, 36] for more details.

In any case as above, the fully discrete scheme can be obtained by applying the third-order TVD Runge-Kutta time discretization method [14]

$$\begin{cases} \boldsymbol{u}^{(1)} = \boldsymbol{u}^n + \Delta t L(\boldsymbol{u}^n), \\ \boldsymbol{u}^{(2)} = \dfrac{3}{4}\boldsymbol{u}^n + \dfrac{1}{4}\boldsymbol{u}^{(1)} + \dfrac{1}{4}\Delta t L(\boldsymbol{u}^{(1)}), \\ \boldsymbol{u}^{n+1} = \dfrac{1}{3}\boldsymbol{u}^n + \dfrac{2}{3}\boldsymbol{u}^{(2)} + \dfrac{2}{3}\Delta t L(\boldsymbol{u}^{(2)}), \end{cases} \tag{10}$$

where L is the spatial discrete operator given by (4) or (6).

2.2 The WENO Reconstruction

Next, we introduce the WENO reconstruction procedure to obtain $h_{i+\frac{1}{2}}$ from the cell average $\bar{h}_i$ of the sliding function. Generally, let $\{\bar{v}_i\}$ be the cell average of a function $v(x)$ on the uniform grid above. In the fifth-order case, for each following stencil:

$$S_k = \{I_{i-3+k}, I_{i-2+k}, I_{i-1+k}\}, k = 1, 2, 3, \tag{11}$$

there is a unique quadratic polynomial denoted by $p_k(x)$ satisfying

$$\frac{1}{\Delta x}\int_{x_{j-\frac{1}{2}}}^{x_{j+\frac{1}{2}}} p_k(\xi)\mathrm{d}\xi = \bar{v}_j, j = i-3+k, i-2+k, i-1+k. \tag{12}$$

Besides, there is a fourth-degree polynomial denoted by $P^L(x)$ satisfying

$$\frac{1}{\Delta x}\int_{x_{j-\frac{1}{2}}}^{x_{j+\frac{1}{2}}} P^L(\xi)\mathrm{d}\xi = \bar{v}_j, j = i-2, i-1, \cdots, i+2. \tag{13}$$

Evaluate $p_k(x)$ at $x_{i\pm\frac{1}{2}}$, we obtain the third-order approximations to $v(x_{i\pm\frac{1}{2}})$ denoted by $p_k(x_{i\pm\frac{1}{2}}) = v^k_{i\pm\frac{1}{2}}, k = 1, 2, 3$. Let $D_k(x)$ be the linear weights satisfying

$$P^L(x) = \sum_{k=1}^{3} D_k(x)p_k(x) = v(x) + \mathcal{O}(\Delta x^5), \tag{14}$$

and take $d_k = D_k(x_{i+\frac{1}{2}}), \tilde{d}_k = D_k(x_{i-\frac{1}{2}}), k = 1, 2, 3$. The explicit values for d_k $(k = 1, 2, 3)$ are $\frac{1}{10}$, $\frac{6}{10}$, and $\frac{3}{10}$, respectively, and $\frac{3}{10}$, $\frac{6}{10}$, $\frac{1}{10}$ for $\tilde{d}_k$. The smoothness indicators β_k $(k = 1, 2, 3)$ in the WENOJS reconstruction are computed by

$$\beta_k = \sum_{r=1}^{2} \Delta x^{2r-1} \int_{x_{i-\frac{1}{2}}}^{x_{i+\frac{1}{2}}} (p_k^{(r)}(x))^2 \mathrm{d}x, \tag{15}$$

where the superscript (r) represents the order of derivative. The nonlinear weights are given by

$$\mu_k(x) = \frac{D_k(x)}{(\epsilon + \beta_k)^p}, \gamma_k(x) = \frac{\mu_k(x)}{\mu_1(x) + \mu_2(x) + \mu_3(x)}, k = 1, 2, 3; \tag{16}$$

$\mu_k(x)$ are the non-normalized nonlinear weights, and $\gamma_k(x)$ are the normalized nonlinear weights. The parameter ϵ is set as 10^{-6} to avoid the denominator becoming zero and reduce the influence from critical points. The parameter p is set as 2 to provide enough weights to smooth stencils. Take $w_k = \gamma_k(x_{i+\frac{1}{2}}), \tilde{w}_k = \gamma_k(x_{i-\frac{1}{2}}), k = 1, 2, 3$, the WENO reconstruction polynomial $P^N(x)$ is given by

$$P^N(x) = \sum_{k=1}^{3} \gamma_k(x) p_k(x), \tag{17}$$

and the final fifth-order approximations at cell boundaries are given by

$$v^-_{i+\frac{1}{2}} = \sum_{k=1}^{3} w_k v^k_{i+\frac{1}{2}}, v^+_{i-\frac{1}{2}} = \sum_{k=1}^{3} \tilde{w}_k v^k_{i-\frac{1}{2}}. \tag{18}$$

In the finite difference method, the numerical fluxes are taken as $\hat{f}^+_{i+\frac{1}{2}} = v^-_{i+\frac{1}{2}}$ by identifying $\bar{v}_i = f^+(u_i)$, and $\hat{f}^-_{i+\frac{1}{2}} = v^+_{i+\frac{1}{2}}$ with $\bar{v}_i = f^-(u_i)$.

The explicit formulas for β_k are

$$\beta_1 = \frac{13}{12}(\bar{v}_{i-2} - 2\bar{v}_{i-1} + \bar{v}_i)^2 + \frac{1}{4}(\bar{v}_{i-2} - 4\bar{v}_{i-1} + 3\bar{v}_i)^2, \tag{19}$$

$$\beta_2 = \frac{13}{12}(\bar{v}_{i-1} - 2\bar{v}_i + \bar{v}_{i+1})^2 + \frac{1}{4}(\bar{v}_{i-1} - \bar{v}_{i+1})^2, \tag{20}$$

$$\beta_3 = \frac{13}{12}(\bar{v}_i - 2\bar{v}_{i+1} + \bar{v}_{i+2})^2 + \frac{1}{4}(3\bar{v}_i - 4\bar{v}_{i+1} + \bar{v}_{i+2})^2. \tag{21}$$

By performing the Taylor expansion at x_i, we have

$$\beta_1 = \bar{v}_i'^2 \Delta x^2 + \left(\frac{13}{12}\bar{v}_i''^2 - \frac{2}{3}\bar{v}_i'\bar{v}_i'''\right)\Delta x^4 - \left(\frac{13}{6}\bar{v}_i''\bar{v}_i''' - \frac{1}{2}\bar{v}_i'\bar{v}_i''''\right)\Delta x^5 + \mathcal{O}\big(\Delta x^6\big), \tag{22}$$

$$\beta_2 = \bar{v}_i'^2 \Delta x^2 + \left(\frac{13}{12}\bar{v}_i''^2 + \frac{1}{3}\bar{v}_i'\bar{v}_i'''\right)\Delta x^4 + \mathcal{O}\big(\Delta x^6\big), \tag{23}$$

$$\beta_3 = \overline{v}_i'^2 \Delta x^2 + \left(\frac{13}{12} \overline{v}_i''^2 - \frac{2}{3} \overline{v}_i' \overline{v}_i''' \right) \Delta x^4 + \left(\frac{13}{6} \overline{v}_i'' \overline{v}_i''' - \frac{1}{2} \overline{v}_i' \overline{v}_i'''' \right) \Delta x^5 + \mathcal{O}\left(\Delta x^6 \right). \quad (24)$$

Compared with the WENOJS reconstruction, the only difference for the WENOZ reconstruction is the use of novel nonlinear weights. Let $\tau_5 = |\beta_1 - \beta_3|$, and the nonlinear weights are given by

$$\mu_k(x) = D_k(x) \left(1 + \left(\frac{\tau_5}{\epsilon + \beta_k} \right)^p \right), \gamma_k(x) = \frac{\mu_k(x)}{\mu_1(x) + \mu_2(x) + \mu_3(x)}, k = 1, 2, 3, \quad (25)$$

and take $w_k = \gamma_k(x_{i+\frac{1}{2}}), \tilde{w}_k = \gamma_k(x_{i-\frac{1}{2}}), k = 1, 2, 3$. The parameter p is set as 2, which can adjust the final weights assigned to smooth and non-smooth stencils. From (22) and (24), it is easy to get

$$\tau_5 = \frac{13}{3} |f_i'' f_i'''| \Delta x^5 + \mathcal{O}(\Delta x^6). \quad (26)$$

The ϵ arising in the nonlinear weight can be taken as $\epsilon = \Delta x^l (l \leqslant 5 - \frac{3}{p})$, and then, we obtain the sufficient condition

$$\gamma_k(x) - D_k(x) = \mathcal{O}(\Delta x^3), \quad (27)$$

which guarantees that the WENOZ scheme maintains the fifth-order accuracy near extrema regardless of the order of critical points.

As pointed out by Borgers et al. [5], by tuning the parameter p, we can recover the accuracy near critical points, while larger p gives larger dissipation. Compared with the WENOJS scheme, the weight assigned to the non-smooth stencil is larger. Besides, near critical points, the nonlinear weight can often recover its linear weight better than the WENOJS scheme. Numerical experiments demonstrate that the WENOZ scheme can give a numerical solution with less dissipation and higher resolution. It is also popular to adopt the hybrid approach to reduce the dissipation and increase the resolution in the reconstruction.

3 The Hybrid Reconstruction Method

In this section, we propose a new hybrid method to perform the reconstruction. The major difference from the existing hybrid strategies is that the domain is classified into three parts: smooth region, non-smooth region, and high-frequency region. In the smooth region, the linear reconstruction is used and the nonlinear WENO reconstruction in the non-smooth region. Meanwhile, a mixed reconstruction of the linear and nonlinear reconstruction is adopted in the high-frequency region for higher resolution.

First, we need to propose some smoothness detectors to identify these sub-stencils. Based on the smoothness detector, if all sub-stencils are "smooth", then the big stencil is marked as smooth region. If all sub-stencils are "non-smooth", then the big stencil is marked as high-frequency region. Otherwise, the stencil is labeled as non-smooth region. There are many different ways to give the smoothness detectors in the hybrid methods. In this paper, we still adopt the smoothness indicator (15) in the WENOJS reconstruction as the major ingredient in the smoothness detector. This approach may not be the most sharp one but a simple and effective choice.

For the fifth-order method, let $\beta^A = \min(\beta_1, \beta_2, \beta_3)$ and $\beta^M = \frac{1}{3}\sum_{i=1}^{3} \beta_i$, where β_i $(i = 1, 2, 3)$ are the smoothness indicators of the sub-stencils in the WENOJS reconstruction. In the smooth region, we have $\tau_5 < \beta^M$, since $\tau_5 = \Delta x^5$, and $\beta^M = \Delta x^2$ if there are no critical points, where $\tau_5 = |\beta_1 - \beta_3|$ is the indicator used in the WENOZ reconstruction. To exclude the influence of critical points, the smooth region is identified by $\tau_5 \leqslant C\Delta x^2$ or $\tau_5 \leqslant \beta^M$. Otherwise, the region is either non-smooth or high-frequency. The high-frequency region is further identified by $\beta^A > C\Delta x$ and the rest is the non-smooth region. The scaling constant C is defined by

$$C = \max\{U_j^2 : j = i-2, i-1, \cdots, i+2\} + 10^{-40}, \tag{28}$$

where U is the variable under reconstruction and the constant 10^{-40} is added to avoid it becoming zero. The parameter $C = \max\{U^2\} + 10^{-40}$ is chosen to make the scheme scale-free. Meanwhile, we found that taking $C = 1$ does not cause any trouble at least in our numerical tests and can get very similar numerical results, which indicate that the scheme is not very sensitive to this parameter. Thus, in numerical tests, the scaling parameter is set as $C = 1$ for simplicity unless otherwise stated.

As mentioned before, for hybrid methods, different approximations are adopted in different regions. Usually, the WENO-type approximation is used to preserve the ENO property in the non-smooth region, and the high-order linear approximation is taken to obtain high resolution and better spectral approximation. Unlike other hybrid methods, now, we have the additional high-frequency region. To increase the spectral resolution and stability, a mixed approximation of the linear and nonlinear methods is proposed as follows.

In the fifth-order method, we can choose the fifth-order linear approximation in (13), and its smoothness indicator is denoted by β^L and computed by (15). In the high-frequency region, the mixed approximation is the convex combination of the linear and WENO approximations with the weights of w_1 and w_2, respectively. The weights are computed by

$$w_1 = \min\left(1, \frac{1 + \sqrt{1 + (a+1)(Q-1)}}{a+1}\right), \; w_2 = 1 - w_1, \tag{29}$$

where $a = \frac{\beta^L}{\beta^A}$. Let P^L and P^N be the fifth-order linear and the WENO polynomials with the smoothness indicators β^L and β^N, respectively. By adopting this pair of weights (w_1, w_2), we can make a conclusion that the smoothness indicator of the combined polynomial is no more than $2Q\beta^N$. It can be justified as follows.

The smoothness indicator of the combined polynomial can be written as

$$\beta^W = \sum_{j=1}^{4} \Delta x^{2j-1} \int_{x_{i-\frac{1}{2}}}^{x_{i+\frac{1}{2}}} ((w_1 P^L + w_2 P^N)^{(j)})^2 \mathrm{d}x. \tag{30}$$

Thus, we have

$$\beta^W \leqslant 2\sum_{j=1}^{4} \Delta x^{2j-1} \int_{x_{i-\frac{1}{2}}}^{x_{i+\frac{1}{2}}} \big(((w_1 P^L)^{(j)})^2 + ((w_2 P^N)^{(j)})^2\big)\mathrm{d}x = 2(w_1^2 \beta^L + w_2^2 \beta^N). \tag{31}$$

We will get $\beta^W \leqslant 2Q\beta^N$ as long as $2(w_1^2\beta^L + w_2^2\beta^N) \leqslant 2Q\beta^N$. Since $0 < \beta^A \leqslant \beta^N$ and $a = \frac{\beta^L}{\beta^A}$, it suffices to let

$$w_1^2 a + w_2^2 = Q. \tag{32}$$

Substitute w_2 with $1 - w_1$, the conclusion follows by solving a one variable quadratic equation:

$$(a+1)w_1^2 - 2w_1 + 1 - Q = 0. \tag{33}$$

Denote $F(a,Q) = \frac{1+\sqrt{1+(a+1)(Q-1)}}{a+1}$. It can be seen that F is an increasing function of Q and a decreasing function of a, which can adaptively adjust the weights according to the flow field information. When $a \leqslant Q$, the weight $w_1 = 1$ for $F(Q,Q) = 1$, and thus, the linear approximation is dominant. Through the parameter Q, we can control the usage of linear approximation in the high-frequency region.

Finally, we summarize our fifth-order hybrid reconstruction procedure as follows.

Algorithm 1 Procedure for the hybrid reconstruction

i) **Procedure** WENO-H
ii) Given the cell averages $\overline{v}_j$ for all j
iii) Calculate β_i, $i = 1,2,3$, β^A, β^M and τ_5
iv) **if** $\tau_5 \leqslant C\Delta x^2$ or $\tau_5 \leqslant \beta^M$ **then**
v) Perform the linear reconstruction
vi) **else if** $\beta^A > C\Delta x$ **then**
vii) Perform the mixed reconstruction
viii) **else**
ix) Perform the WENO reconstruction

In this paper, we apply the hybrid approach on the fifth-order WENOJS and WENOZ finite difference schemes, respectively, named as WENOJS-H and WENOZ-H schemes. To examine the performances of schemes with/without the hybridization, we adopt the approach in [28–30] to compare the approximate dispersion and dissipation relations with the fifth-order linear (LIN5) reconstruction. Let w, w' be the reduced wave number and the modified wave number, respectively. The results are shown in Figs. 1 and 2, which demonstrate that the new hybrid schemes maintain lower dispersion and dissipation errors than the original schemes. Without the hybrid procedure, the WENOZ scheme shows

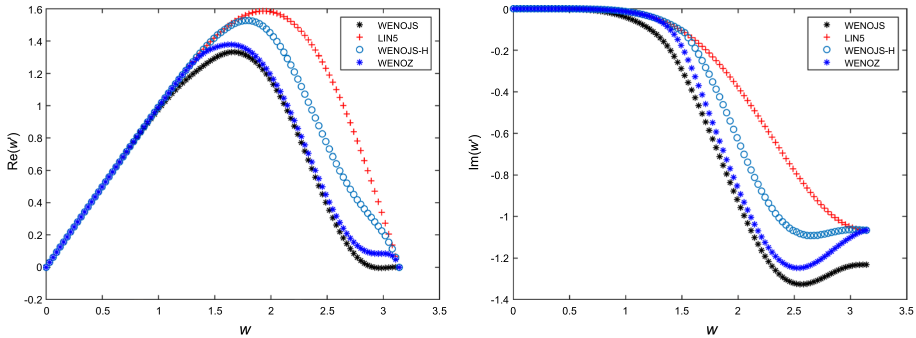

(a) Dispersion **(b)** Dissipation

Fig. 1 Approximate dispersion and dissipation relations for WENOJS-type schemes

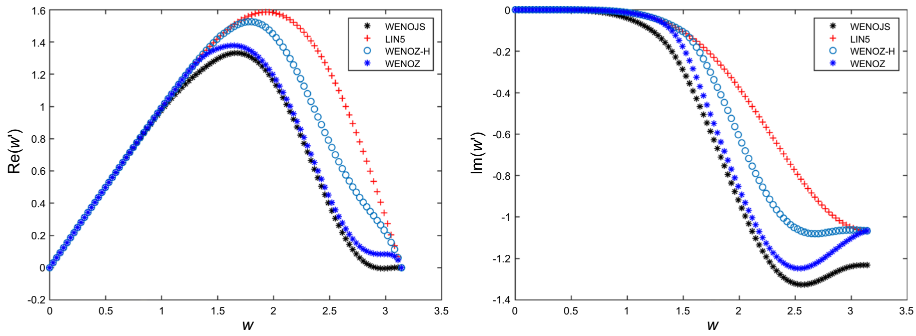

(a) Dispersion **(b)** Dissipation

Fig. 2 Approximate dispersion and dissipation relations for WENOZ-type schemes

slightly better performance than the WENOJS scheme. After the hybridization, both hybrid schemes perform very similarly to each other, but much better performance than the original ones. The similar observation can be found in other numerical tests in the following section.

In this approximate spectral analysis, we take $\epsilon = 10^{-6}, p = 2$ for WENOJS and WENOZ schemes, and $Q = 9$ for both hybrid schemes. And the scaling parameter is set as $C = 1$ for simplicity, which is not sensitive in the schemes. In the rest of numerical tests, the same parameters are adopted unless otherwise stated.

4 Numerical Results

In this section, we present the numerical results of the fifth-order WENOJS and WENOZ finite difference schemes and the corresponding hybrid WENOJS-H and WENOZ-H schemes. The third-order Runge-Kutta method (10) [14] is used to march in time and the CFL number is set as 0.6. Unless specified, we always take $\epsilon = 10^{-6}, p = 2$ in all WENO schemes for fair comparison and keep $Q = 9$ and $C = 1$ in all the hybrid schemes. In the accuracy tests, we take $\Delta t \approx \Delta x^{\frac{5}{3}}$ to make sure that the spatial error dominates.

Example 1

(a) We approximate the following functions by the reconstruction algorithms of the fifth-order WENOJS, WENOJS-H, and linear (LIN5) reconstruction:

$$u_1(x) = 1 + 3\sin(7x), 0 < x < 2\pi, \tag{34}$$

$$u_2(x) = \begin{cases} 1 + 3\sin(7x), 0 < x < 2, \\ 3\sin(7x), \quad 2 < x < 5, \\ 1 + 3\sin(7x), 5 < x < 2\pi. \end{cases} \tag{35}$$

The numerical results are shown in Fig. 3. It can be seen that the hybrid reconstruction becomes the linear reconstruction and gives less error than original WENOJS

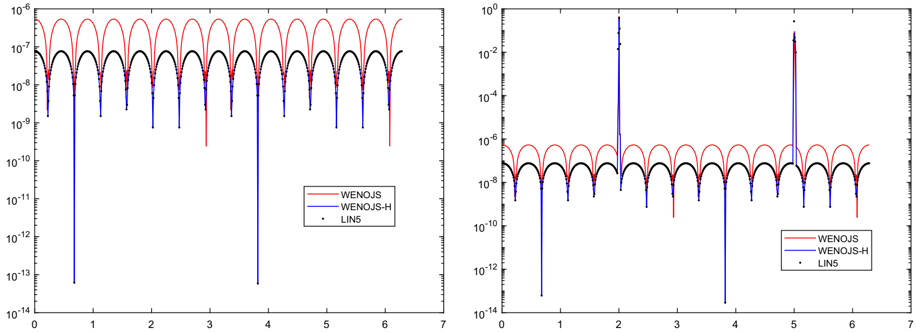

Fig. 3 Numerical results of WENOJS-type schemes, uniform mesh with 640 cells. Left: error distributions for $u_1(x)$; right: error distributions for $u_2(x)$

reconstruction in most region. Near the discontinuities, the hybrid approach maintains the similar resolution as the WENOJS reconstruction. The WENOZ and its hybrid reconstruction perform similarly as the linear scheme, and thus, we omit it here.

(b) We approximate the following function [6] by the fifth-order WENOZ, WENOZ-H, and linear reconstruction algorithms:

$$u_3(x) = \mathrm{e}^{2x}x^3, -1 < x < 1. \tag{36}$$

In Fig. 4, it shows that the hybrid reconstruction becomes the linear reconstruction in this case and gives less error than original WENOZ reconstruction near critical point.

Example 2 Consider the linear convection equation

$$u_t + u_x = 0 \tag{37}$$

with the initial condition $u(x, 0) = \sin x$ and the periodic boundary condition. We compute the numerical solution till $T = 0.5$. The errors for different schemes are shown in Figs. 5

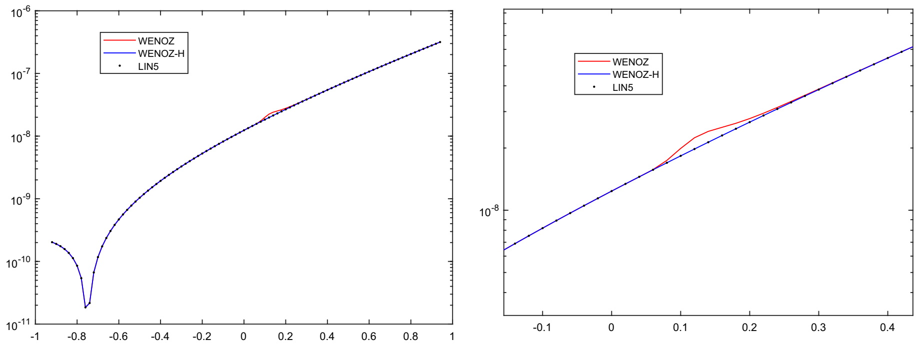

Fig. 4 Numerical results of WENOZ-type schemes, uniform mesh with 100 cells. Left: error distributions for $u_3(x)$; right: zoomed-in error distributions near critical point for $u_3(x)$

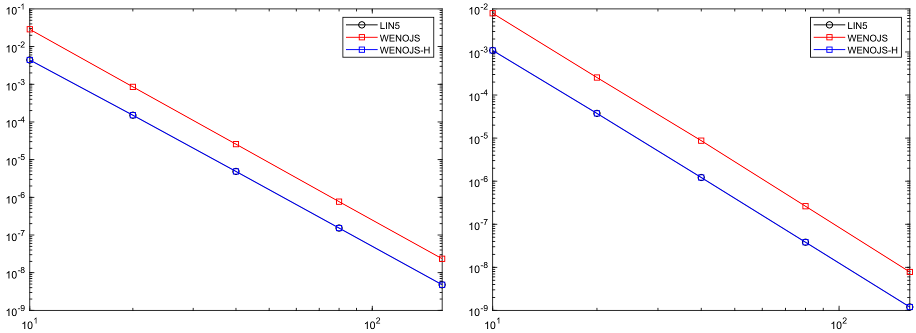

Fig. 5 Accuracy test of 1D scalar convection equation for the WENOJS-type schemes. Uniform meshes with $N = 10, 20, 40, 80, 160$ cells at time $T = 0.5$. Left: L^1 errors for the WENOJS-type schemes; right: L^∞ errors for the WENOJS-type schemes

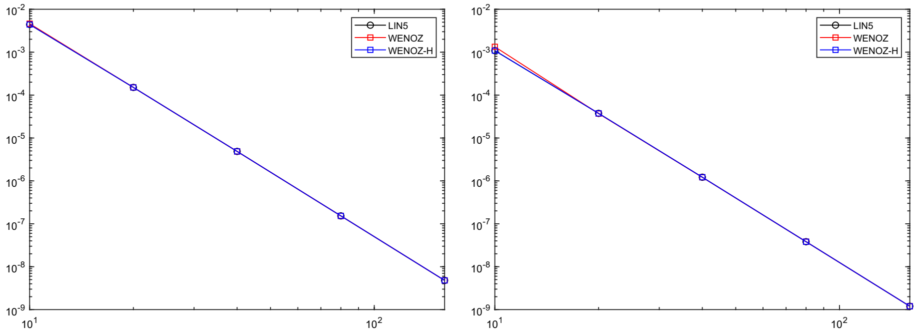

Fig. 6 Accuracy test of 1D scalar convection equation for the WENOZ-type schemes. Uniform meshes with $N = 10, 20, 40, 80, 160$ cells at time $T = 0.5$. Left: L^1 errors for the WENOZ-type schemes; right: L^∞ errors for the WENOZ-type schemes

and 6. We can see that the WENOJS-H scheme presents solution with less error than the original scheme, while the WENOZ-H scheme presents solution with less error than the original scheme on the coarse grid. Next, we solve the same Eq. (37) with the discontinuous initial condition

$$u(x,0) = \begin{cases} \sin x, & 0 < x < 2, \\ \sin x - 1, & 2 < x < 5, \\ \sin x, & 5 < x < 2\pi. \end{cases} \tag{38}$$

There are two discontinuities in the domain. We compute the numerical solution till $T = 2\pi$. In Fig. 8, the time history of different regions is shown. The numerical results and error distributions for different schemes are shown in Fig. 7, which shows that the hybrid schemes maintain the same resolution as the original WENO schemes near discontinuities.

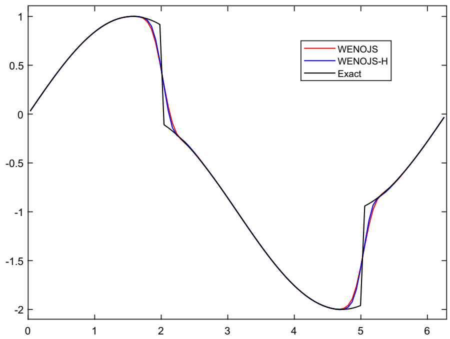

(a) WENOJS **(b)** WENOZ

Fig. 7 Numerical results for the 1D scalar convection equation. Uniform mesh with 100 cells at time $T = 2\pi$

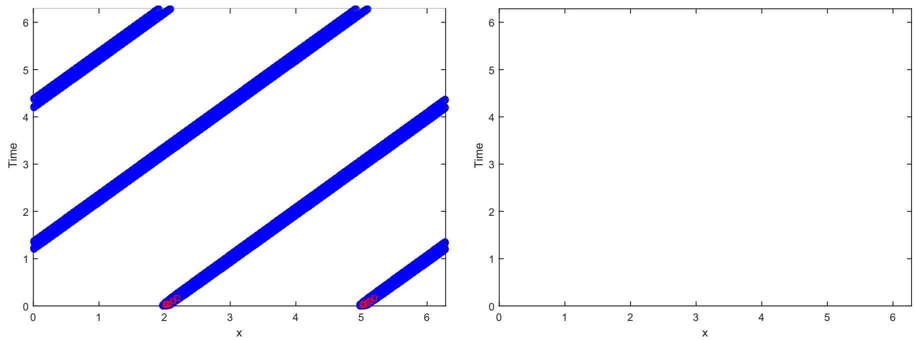

(a) $\hat{f}^{+}_{i+\frac{1}{2}}$ **(b)** $\hat{f}^{-}_{i+\frac{1}{2}}$

Fig. 8 The time history of different regions of the numerical solution computed by the WENOZ-H scheme for the 1D scalar convection equation (only the center cell is marked). Uniform mesh with 320 cells till time $T = 2\pi$. Blue circles: marks of non-smooth region; red squares: marks of high-frequency region

Example 3 Consider the one-dimensional Burgers equation

$$u_t + \left(\frac{u^2}{2}\right)_x = 0,\ 0 < x < 2\pi \tag{39}$$

with the initial condition $u(x,0) = \frac{1}{2} + \sin x$ and the periodic boundary condition. We compute the numerical solution till $T = 0.5$ when the solution is still smooth. In Fig. 12, the time history of different regions is provided. The numerical results are shown in Figs. 9 and 10. We can see that both hybrid schemes generate numerical solutions with less error than the original schemes. Then, we compute the numerical solution till $T = 1.5$ when the shock appears. The numerical results for different schemes are shown in Fig. 11; all the schemes generate oscillation free solution.

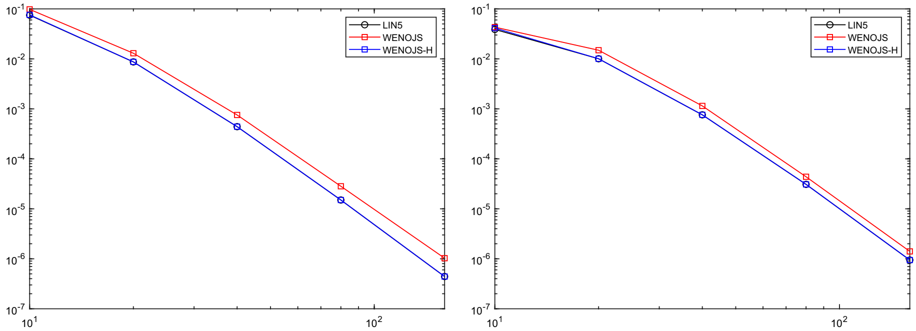

Fig. 9 Accuracy test of 1D scalar Burgers equation for the WENOJS-type schemes. Uniform meshes with $N = 10, 20, 40, 80, 160$ cells at time $T = 0.5$. Left: L^1 errors for the WENOJS-type schemes; right: L^∞ errors for the WENOJS-type schemes

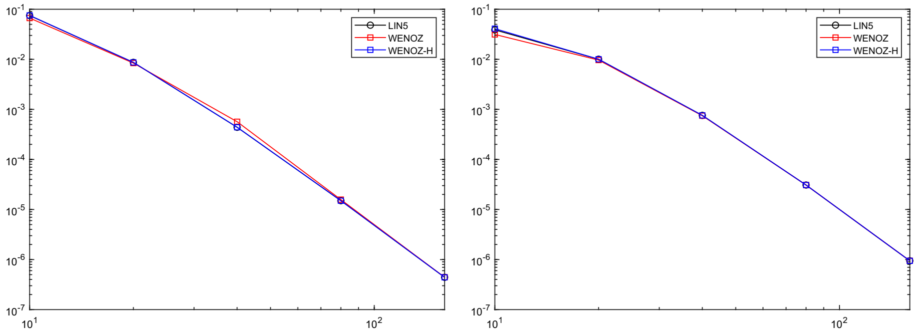

Fig. 10 Accuracy test of 1D scalar Burgers equation for the WENOZ-type schemes. Uniform meshes with $N = 10, 20, 40, 80, 160$ cells at time $T = 0.5$. Left: L^1 errors for the WENOZ-type schemes; right: L^∞ errors for the WENOZ-type schemes

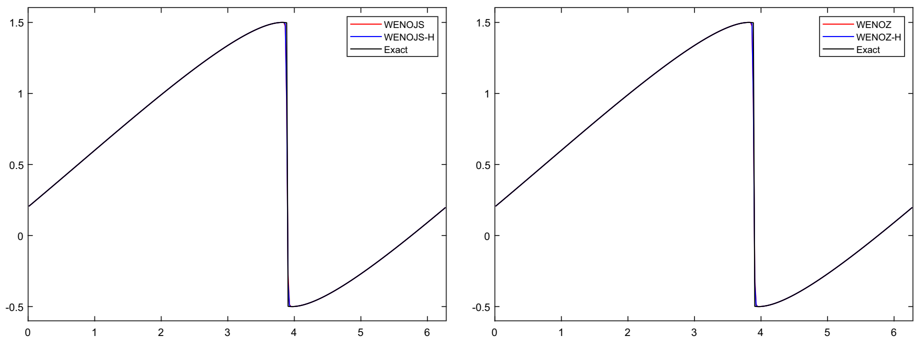

(a) WENOJS **(b)** WENOZ

Fig. 11 Numerical results for the 1D scalar Burgers equation. Uniform mesh with 300 cells at time $T = 1.5$

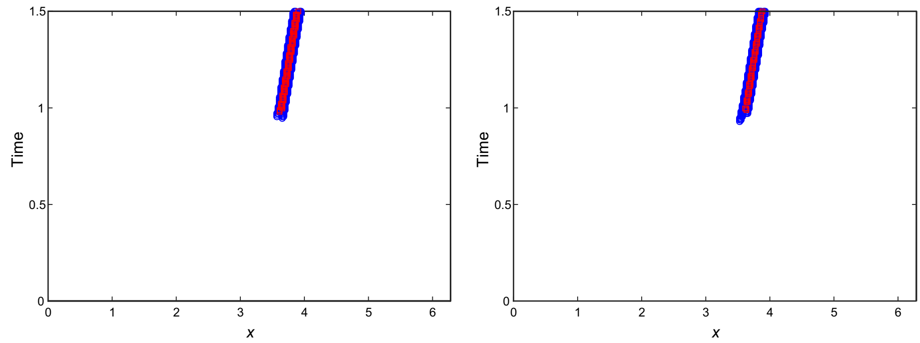

(a) $\hat{f}^{+}_{i+\frac{1}{2}}$ **(b)** $\hat{f}^{-}_{i+\frac{1}{2}}$

Fig. 12 The time history of different regions of the numerical solution computed by the WENOZ-H scheme for the 1D scalar Burgers equation (only the center cell is marked). Uniform mesh with 300 cells till time $T = 1.5$. Blue circles: marks of non-smooth region; red squares: marks of high-frequency region

Example 4 We solve the 2D scalar convection equation

$$u_t + u_x + u_y = 0, (x, y) \in [0, 1]^2 \tag{40}$$

with the initial condition

$$u(x, 0) = \begin{cases} \sin(2\pi(x + y)) - 1, (x - 0.5)^2 + (y - 0.5)^2 < \dfrac{1}{8}, \\ \sin(2\pi(x + y)), \quad \text{otherwise}, \end{cases} \tag{41}$$

and the periodic boundary condition. We compute the numerical solution till $T = 0.1$. The numerical results are shown in Figs. 13 and 14. It is found that all the schemes generate oscillation-free solution, while the hybrid schemes give slightly less error than original schemes near discontinuities.

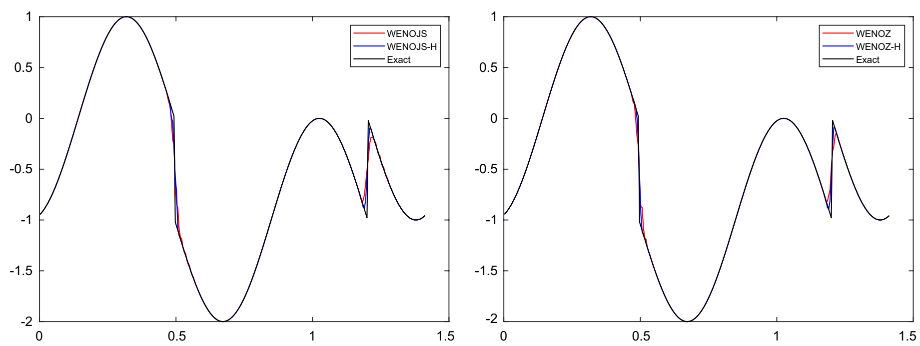

(a) WENOJS **(b)** WENOZ

Fig. 13 1D cut along diagonal for the 2D scalar convection equation. Uniform mesh with 300×300 cells at time $T = 0.1$

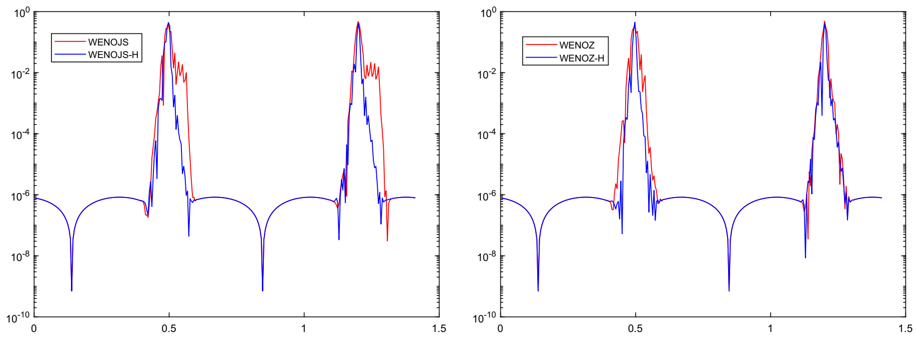

(a) WENOJS **(b)** WENOZ

Fig. 14 Error distributions along diagonal for the 2D scalar convection equation. Uniform mesh with 300×300 cells at time $T = 0.1$

Example 5 We solve the 2D scalar Burgers equation

$$u_t + \left(\frac{u^2}{2}\right)_x + \left(\frac{u^2}{2}\right)_y = 0, (x, y) \in [-2, 2]^2 \tag{42}$$

with the initial condition $u(x, 0) = 0.5 + \sin(\frac{\pi}{2}(x + y))$, and the periodic boundary condition. We compute the numerical solution till $T = \frac{0.5}{\pi}$ when the solution is still smooth. The numerical results are shown in Figs. 15 and 16. We can see that both the new schemes achieve fifth-order accuracy, while the hybrid schemes give less errors than original schemes especially in coarse grid. We proceed to solve the equation till $T = \frac{1.5}{\pi}$ when shock appears. The numerical results and errors are shown in Figs. 17 and 18. All schemes generate oscillation-free solution.

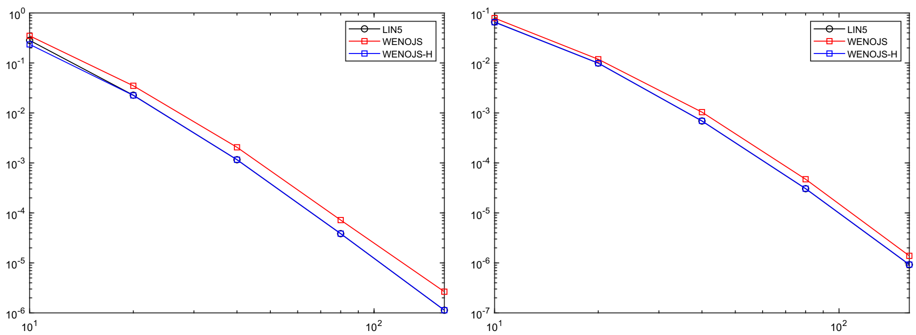

Fig. 15 Accuracy test of 2D scalar Burgers equation for the WENOJS-type schemes. Uniform meshes with $N = 10, 20, 40, 80, 160$ cells at time $T = \frac{0.5}{\pi}$. Left: L^1 errors for the WENOJS-type schemes; right: L^∞ errors for the WENOJS-type schemes

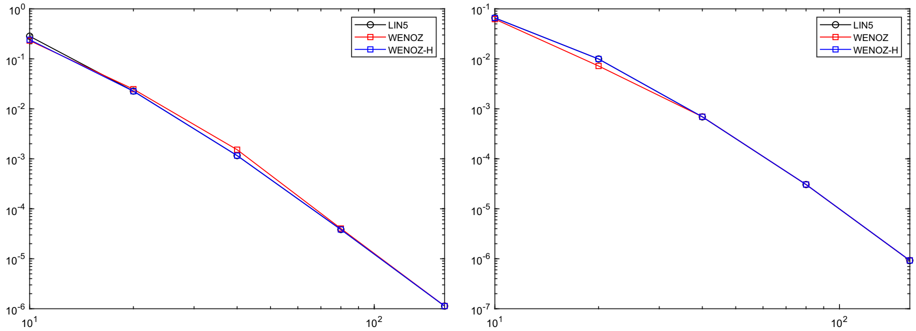

Fig. 16 Accuracy test of 2D scalar Burgers equation for the WENOZ-type schemes. Uniform meshes with $N = 10, 20, 40, 80, 160$ cells at time $T = \frac{0.5}{\pi}$. Left: L^1 errors for the WENOZ-type schemes; right: L^∞ errors for the WENOZ-type schemes

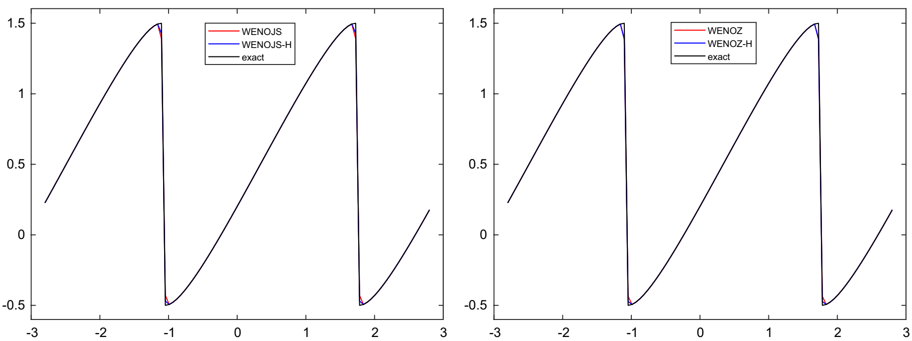

(a) WENOJS **(b)** WENOZ

Fig. 17 1D cut along diagonal for the 2D scalar Burgers equation. Uniform mesh with 100×100 cells at time $T = \frac{1.5}{\pi}$

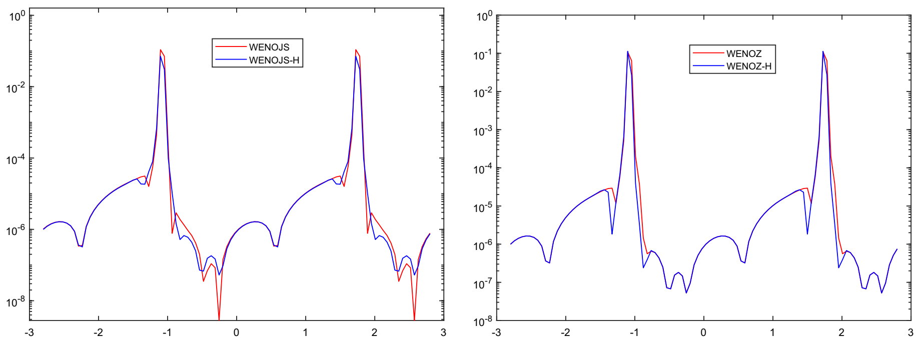

(a) WENOJS **(b)** WENOZ

Fig. 18 Error distributions along diagonal for the 2D scalar Burgers equation. Uniform mesh with 100×100 cells at time $T = \frac{1.5}{\pi}$

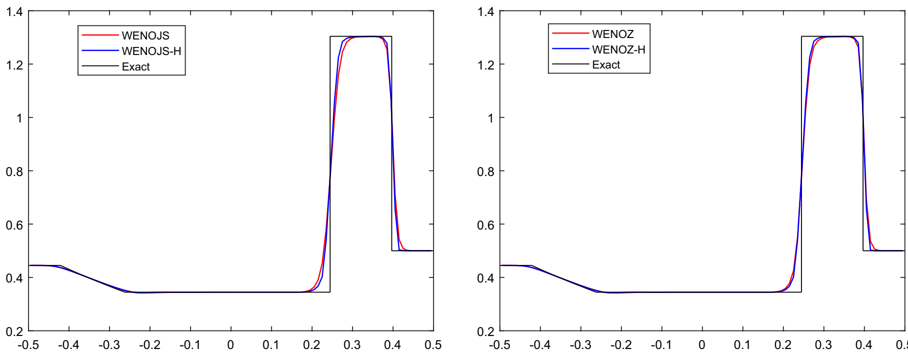

(a) WENOJS **(b)** WENOZ

Fig. 19 Numerical results for the 1D Lax's problem. Uniform mesh with 100 cells at time $T = 0.16$

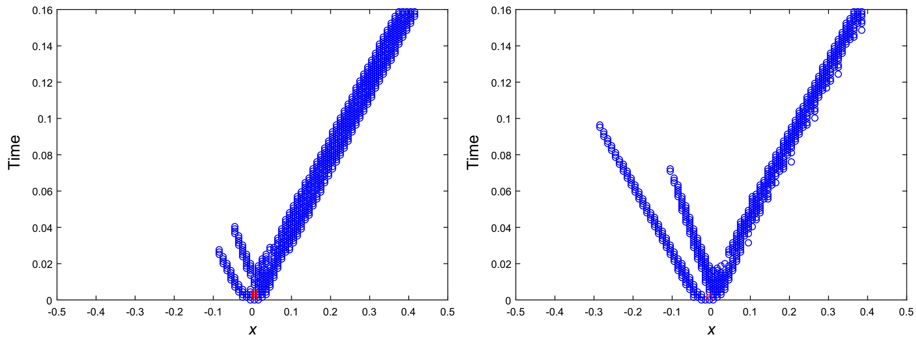

(a) $\hat{f}^{+}_{i+\frac{1}{2}}$ **(b)** $\hat{f}^{-}_{i+\frac{1}{2}}$

Fig. 20 The time history of different regions of the numerical solution computed by the WENOZ-H scheme for the 1D Lax's problem (only the center cell is marked). Uniform mesh with 100 cells till time $T = 0.16$. Blue circles: marks of non-smooth region; red squares: marks of high-frequency region

Example 6 We solve the one-dimensional Euler equation

$$\frac{\partial}{\partial t}\begin{pmatrix}\rho\\ \rho u\\ E\end{pmatrix} + \frac{\partial}{\partial x}\begin{pmatrix}\rho u\\ \rho u^2 + P\\ u(E+P)\end{pmatrix} = \mathbf{0} \tag{43}$$

with the Riemann initial condition for the Lax's problem

$$(\rho, u, P, \gamma)^{\mathrm{T}} = \begin{cases}(0.445, 0.698, 3.528, 1.4)^{\mathrm{T}}, x \in [-0.5, 0),\\ (0.5, 0, 0.571, 1.4)^{\mathrm{T}}, x \in [0, 0.5],\end{cases} \tag{44}$$

where ρ is the density, u is the velocity, P is the pressure, $E = \frac{1}{2}\rho u^2 + \frac{P}{\gamma-1}$, and γ is the ratio of specific heats. We compute the density ρ by the finite difference schemes at $T = 0.16$ in Fig. 19. In Fig. 20, the time history of different regions is shown. It can be seen that all

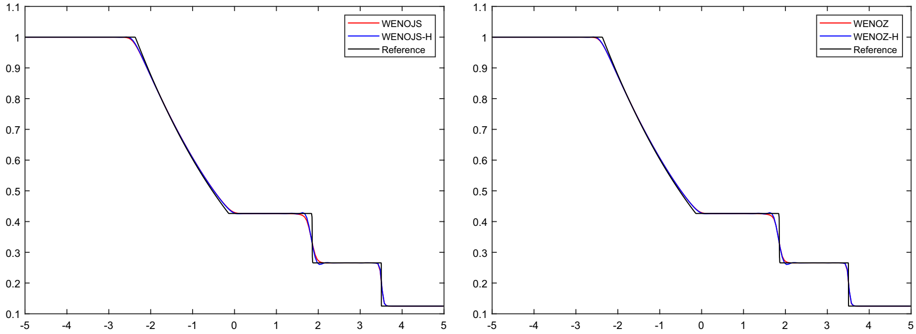

(a) WENOJS **(b)** WENOZ

Fig. 21 Numerical results for the 1D Sod's problem. Uniform mesh with 200 cells at time $T = 2$

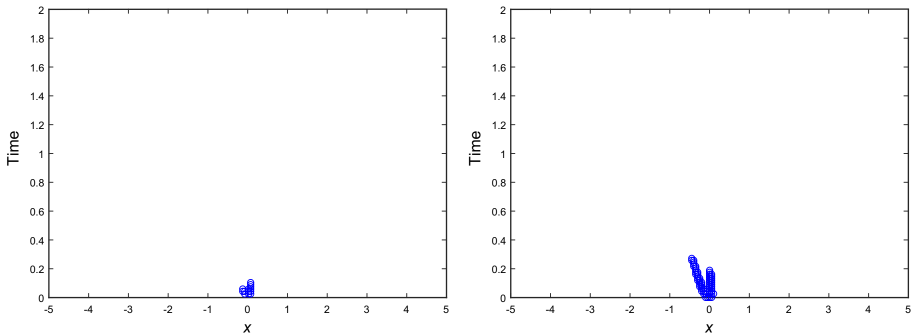

(a) $\hat{f}^{+}_{i+\frac{1}{2}}$ **(b)** $\hat{f}^{-}_{i+\frac{1}{2}}$

Fig. 22 The time history of different regions of the numerical solution computed by the WENOZ-H scheme for the 1D Sod's problem (only the center cell is marked). Uniform mesh with 200 cells till time $T = 2$. Blue circles: marks of non-smooth region; red squares: marks of high-frequency region

schemes generate oscillation-free solution, while the hybrid schemes give slightly sharper approximation near shock and contact discontinuity.

Next, we solve the equations with the Riemann initial condition for the Sod's problem

$$(\rho, u, P, \gamma)^{\mathrm{T}} = \begin{cases} (1, 0, 1, 1.4)^{\mathrm{T}}, & x \in [-5, 0), \\ (0.125, 0, 0.1, 1.4)^{\mathrm{T}}, & x \in [0, 5]. \end{cases} \tag{45}$$

The referenced solution (black line) is the numerical solution computed by the fifth-order finite difference WENOJS scheme with 10 000 grid points. In Fig. 22, the time history of different regions is presented. The density ρ computed at $T = 2$ is plotted in Fig. 21, which shows that all schemes generate essentially oscillation-free solution.

Then, we consider the shock density wave interaction problem in [35] with a moving Mach=3 shock interacting with sine waves in density

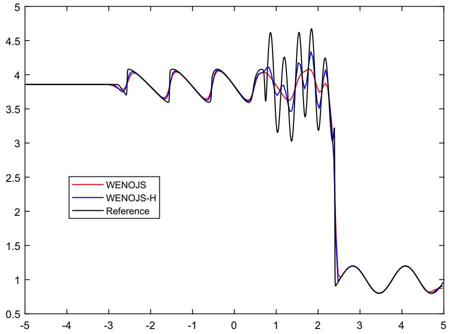

(a) WENOJS **(b)** WENOZ

Fig. 23 Numerical results for the 1D Shu-Osher's problem. Uniform mesh with 200 cells at time $T = 1.8$

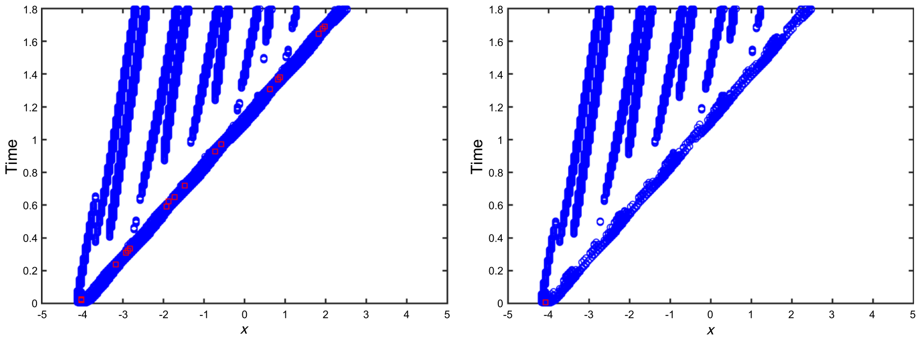

(a) $\hat{f}^{+}_{i+\frac{1}{2}}$ **(b)** $\hat{f}^{-}_{i+\frac{1}{2}}$

Fig. 24 The time history of different regions of the numerical solution computed by the WENOZ-H scheme for the 1D Shu-Osher's problem (only the center cell is marked). Uniform mesh with 200 cells till time $T = 1.8$. Blue circles: marks of non-smooth region; red squares: marks of high-frequency region

$$(\rho, u, P, \gamma)^{\mathrm{T}} = \begin{cases} (3.857\,143, 2.629\,369, 10.333\,333, 1.4)^{\mathrm{T}}, & x \in [-5, -4), \\ (1 + 0.2\sin(5x), 0, 1, 1.4)^{\mathrm{T}}, & x \in [-4, 5]. \end{cases} \tag{46}$$

The referenced solution (black line) is the numerical solution computed by the fifth-order finite difference WENOJS scheme with 2 000 grid points. The final computational time is $T = 1.8$. From Fig. 23, we can see that both hybrid schemes could capture high-frequency wave better than original schemes, and the performance of the hybrid schemes are similar. In Fig. 24, the time history of different regions is shown.

We now consider the interaction of two blast waves. The initial conditions are

$$(\rho, u, P, \gamma)^{\mathrm{T}} = \begin{cases} (1, 0, 10^3, 1.4)^{\mathrm{T}}, x \in (0, 0.1), \\ (1, 0, 10^{-2}, 1.4)^{\mathrm{T}}, x \in (0.1, 0.9), \\ (1, 0, 10^2, 1.4)^{\mathrm{T}}, x \in (0.9, 1). \end{cases} \tag{47}$$

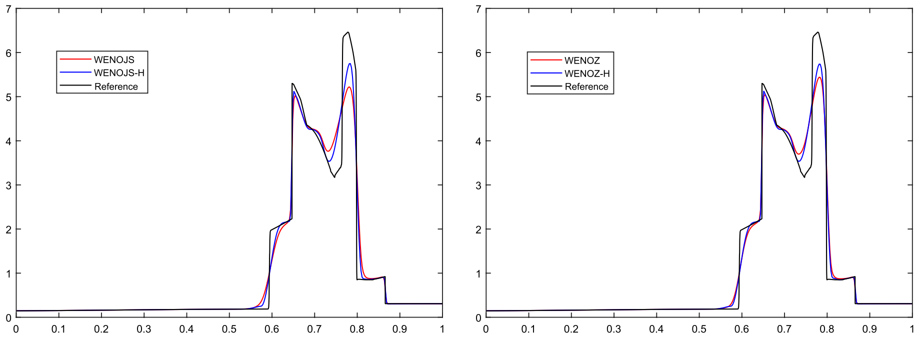

(a) WENOJS **(b)** WENOZ

Fig. 25 Numerical results for the interaction of two blast waves. Uniform mesh with 400 cells at time $T = 0.038$

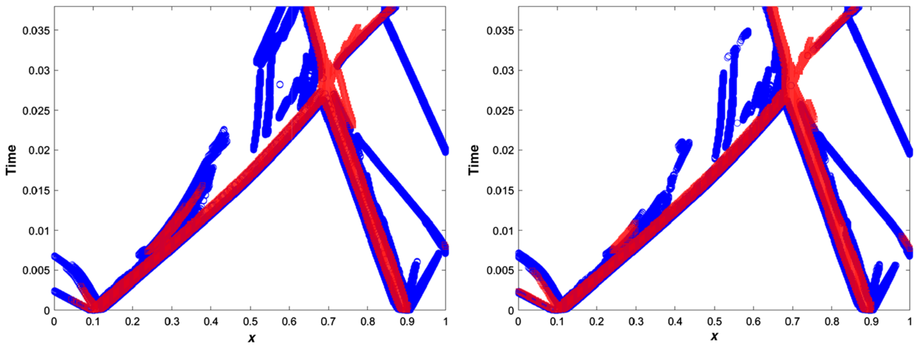

(a) $\hat{f}^{+}_{i+\frac{1}{2}}$ **(b)** $\hat{f}^{-}_{i+\frac{1}{2}}$

Fig. 26 The time history of different regions of the numerical solution computed by the WENOZ-H scheme for the interaction of two blast waves (only the center cell is marked). Uniform mesh with 400 cells till time $T = 0.038$. Blue circles: marks of non-smooth region; red squares: marks of high-frequency region

The numerical solutions are shown in Fig. 25, where the referenced solution (black line) is the numerical solution computed by the fifth-order finite difference WENOZ-H scheme with 20 000 grid points. The final computational time is $T = 0.038$. In Fig. 26, the time history of different regions is given. We can conclude that the hybrid WENOJS-H and WENOZ-H schemes show better resolution than the original WENOJS and WENOZ schemes. And the schemes after hybridization perform similarly.

The last case for 1D Euler equations is the Sedov's blast wave problem [33]. This problem contains strong shocks with very low density. Initially, $\rho = 1, u = 0, E = 10^{-12}$ everywhere except the energy in the center cell is the constant $\frac{3\,200\,000}{\Delta x}$. The referenced solution (black line) is the numerical solution computed by the fifth-order finite difference WENOJS scheme with 4 000 grid points. We compute the numerical solution till $T = 0.001$. From Fig. 27, it can be seen that the hybrid schemes generate numerical solutions with more sharper transition near shocks. By taking $C = 1$, the time history of different regions is presented in Fig. 28. We also give another Fig. 29 to show the time history of different

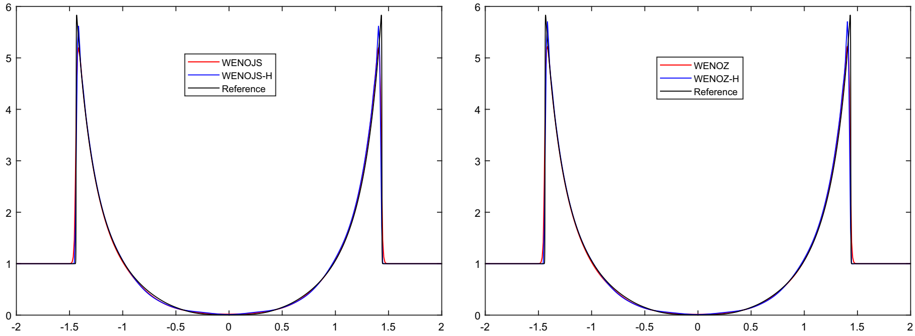

(a) WENOJS **(b)** WENOZ

Fig. 27 Numerical results for the Sedov's blast wave. Uniform mesh with 400 cells at time $T = 0.001$

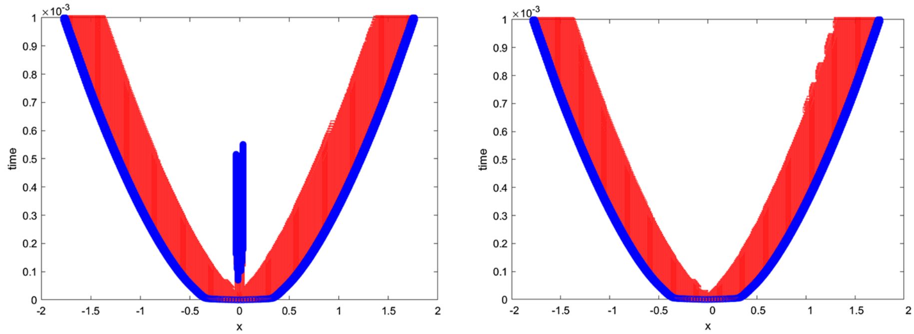

(a) $\hat{f}^{+}_{i+\frac{1}{2}}$ **(b)** $\hat{f}^{-}_{i+\frac{1}{2}}$

Fig. 28 $C = 1$: the time history of different regions of the numerical solution computed by the WENOZ-H scheme for the Sedov's blast wave (only the center cell is marked). Uniform mesh with 400 cells till time $T = 0.001$. Blue circles: marks of non-smooth region; red squares: marks of high-frequency region

regions, where C is determined by (28). For this extreme case, the scheme with $C = 1$ can still give a sharp capture of discontinuities as Fig. 27 shows.

Example 7 Next, we consider the accuracy test for two-dimensional Euler equations

$$\frac{\partial}{\partial t}\begin{pmatrix}\rho\\ \rho u\\ \rho v\\ E\end{pmatrix}+\frac{\partial}{\partial x}\begin{pmatrix}\rho u\\ \rho u^2+P\\ \rho uv\\ u(E+P)\end{pmatrix}+\frac{\partial}{\partial y}\begin{pmatrix}\rho v\\ \rho uv\\ \rho v^2+P\\ v(E+P)\end{pmatrix}=\mathbf{0}, \tag{48}$$

in which ρ is the density, u and v are the velocities in the x and y directions, respectively, $E = \frac{1}{2}\rho(u^2+v^2)+\frac{P}{\gamma-1}$ is the total energy, and P is the pressure.

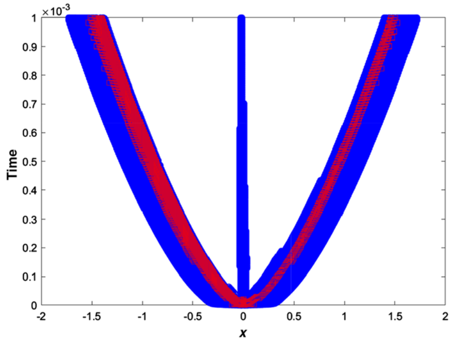

(a) $\hat{f}^+_{i+\frac{1}{2}}$ (b) $\hat{f}^-_{i+\frac{1}{2}}$

Fig. 29 C is determined by (28): the time history of different regions of the numerical solution computed by the WENOZ-H scheme for the Sedov's blast wave (only the center cell is marked). Uniform mesh with 400 cells till time $T = 0.001$. Blue circles: marks of non-smooth region; red squares: marks of high-frequency region

First, we consider the linear degenerate wave. Initially, these variables are set as $\rho(x, y, 0) = 1 + 0.2\sin(x + y), u(x, y, 0) = 1, v(x, y, 0) = 1, P(x, y, 0) = 1$. We compute the numerical solution in $[0, 2\pi]$ with periodic boundary conditions till $T = 0.2$. The exact solution is $\rho(x, y, t) = 1 + 0.2\sin(x + y - 2t)$. The numerical errors are shown in Figs. 30 and 31. All schemes achieve the fifth-order accuracy, while the WENOJS-H scheme presents less absolute error in each grid compared with the original WENOJS scheme. The WENOZ and WENOZ-H schemes perform quite similarly as in the 1D linear convection problem.

Then, we consider the vortex evolution problem. We compute this essential nonlinear problem in $[0, 10]^2$. The mean flow is $\rho = 1, P = 1, (u, v) = (1, 1)$. An isentropic vortex is added with no perturbation in the entropy $S = \frac{P}{\rho^\gamma}$. Let temperature $T = \frac{P}{\rho}$, and the change for the velocities (u, v),T, S can be formulated as follows:

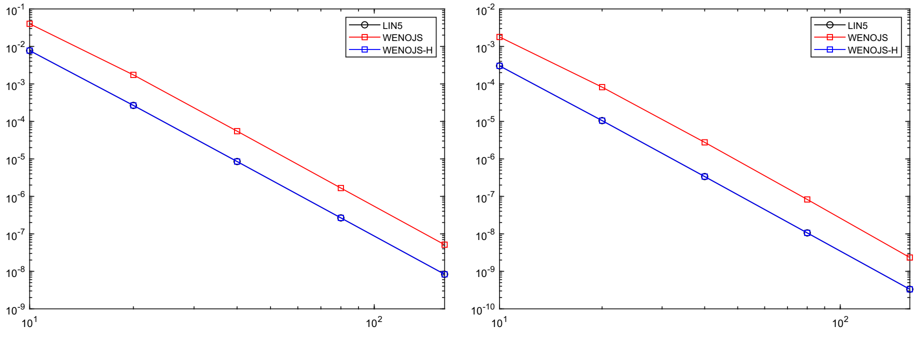

Fig. 30 Accuracy test of 2D Euler equations for the WENOJS-type schemes. Uniform meshes with $N = 10, 20, 40, 80, 160$ cells at time $T = 0.2$. Left: L^1 errors for the WENOJS-type schemes; right: L^∞ errors for the WENOJS-type schemes

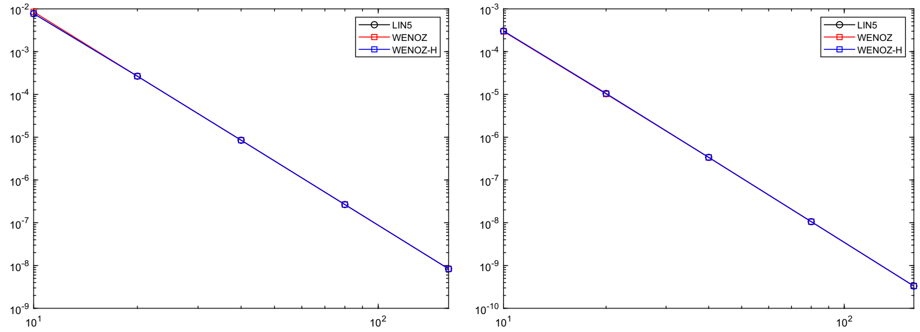

Fig. 31 Accuracy test of 2D Euler equations for the WENOZ-type schemes. Uniform meshes with $N = 10, 20, 40, 80, 160$ cells at time $T = 0.2$. Left: L^1 errors for the WENOZ-type schemes; right: L^∞ errors for the WENOZ-type schemes

$$(\delta u, \delta v) = \frac{\epsilon}{2\pi} \mathrm{e}^{0.5(1-r^2)}(-\bar{y}, \bar{x}), \ \delta T = -\frac{(\gamma-1)\epsilon^2}{8\gamma\pi^2}\mathrm{e}^{1-r^2}, \ \delta S = 0, \tag{49}$$

where $(\bar{x}, \bar{y}) = (x-5, y-5)$, $r^2 = \bar{x}^2 + \bar{y}^2$, and the vortex strength $\epsilon = 5$. The exact solution is the passive convection of the vortex with the mean velocity. We compute the numerical solution with the periodic boundary condition till $T = 0.2$. The numerical results are shown in Figs. 32 and 33. Now, both hybrid WENOJS-H and WENOZ-H schemes generate numerical solution with less error than the WENOJS and WENOZ schemes. And the hybrid schemes perform as well as the linear scheme even on the most coarse grid.

Example 8 Double Mach reflection problem [41, 48, 49]. We compute the numerical solution in a rectangular $[0, 4] \times [0, 1]$. Initially, the computational domain is divided into two parts, and the dividing line lies at the bottom of the domain starting from $x = \frac{1}{6}, y = 0$, making a $60°$ angle with the x-axis. Reflection boundary conditions are imposed for the

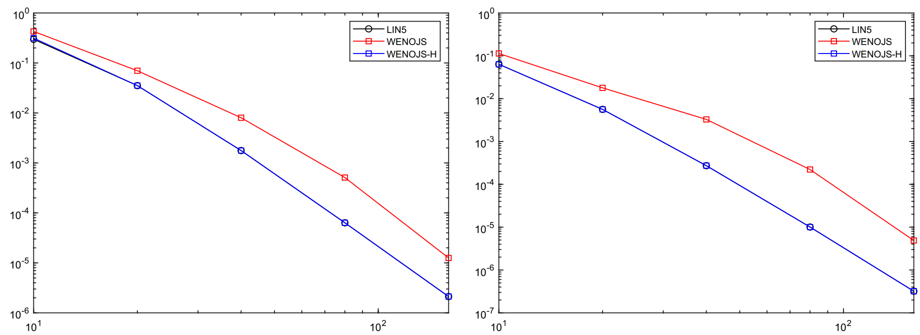

Fig. 32 Accuracy test of 2D vortex evolution for the WENOJS-type schemes. Uniform meshes with $N = 10, 20, 40, 80, 160$ cells at time $T = 0.2$. Left: L^1 errors for the WENOJS-type schemes; right: L^∞ errors for the WENOJS-type schemes

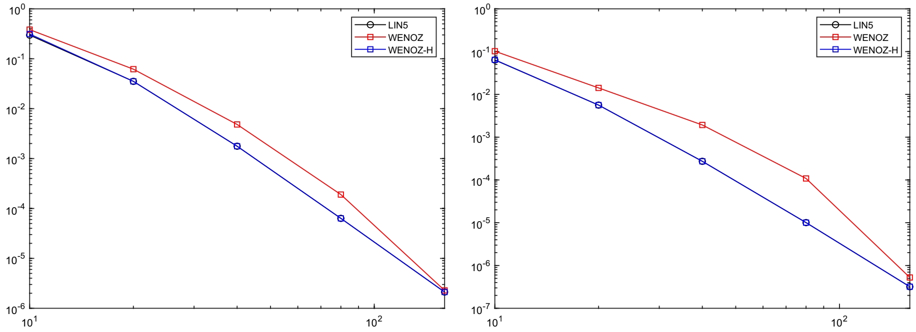

Fig. 33 Accuracy test of 2D vortex evolution for the WENOZ-type schemes. Uniform meshes with $N = 10, 20, 40, 80, 160$ cells at time $T = 0.2$. Left: L^1 errors for the WENOZ-type schemes; right: L^∞ errors for the WENOZ-type schemes

bottom boundary starting from $x = 0$ to $x = \frac{1}{6}$. The top boundary is the exact motion of the Mach 10 shock. The final computational time is $T = 0.2$. We present the contour line of region $[0, 3] \times [0, 1]$ in Fig. 34, and the zoomed-in figure in Fig. 35. Clearly, we can see that the new hybrid WENO schemes capture more details in flow field than WENOJS and WENOZ schemes. And the hybrid schemes perform similarly no matter which original WENO scheme is adopted. The history of ratios of different routes usage in the WENOZ-H scheme is shown in Fig. 36. The *flag* distributions at $T = 0.2$ are shown in Fig. 37, where the symbols $flag_x$ and $flag_y$ represent the detection results checked by the indicator in x- and y-directions, respectively. If $\tau_5 \leqslant C\Delta x^2$ or $\tau_5 \leqslant \beta^M$, then $flag_x = 0$; otherwise, $flag_x = 1$. In the following text, either $flag_x$ or $flag_y$ represents the same meaning. The ratio of $flag_x$ is defined as $\frac{\sum flag_x}{N_x N_y}$, where N_x, N_y are the the number of grid points in x- and y-directions, respectively, and the summation is taken over the whole computational

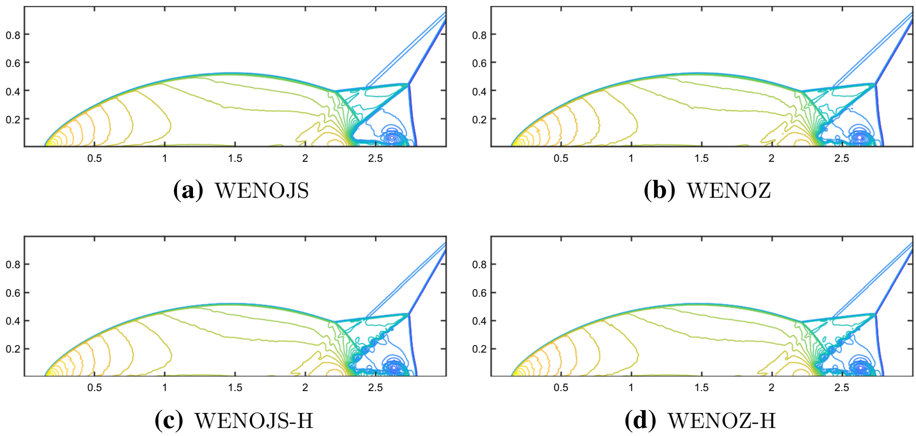

Fig. 34 Numerical results for the double Mach reflection problem. Uniform mesh with 960×240 cells at time $T = 0.2$. Forty-three equally spaced density contours from 1.887 to 22.9

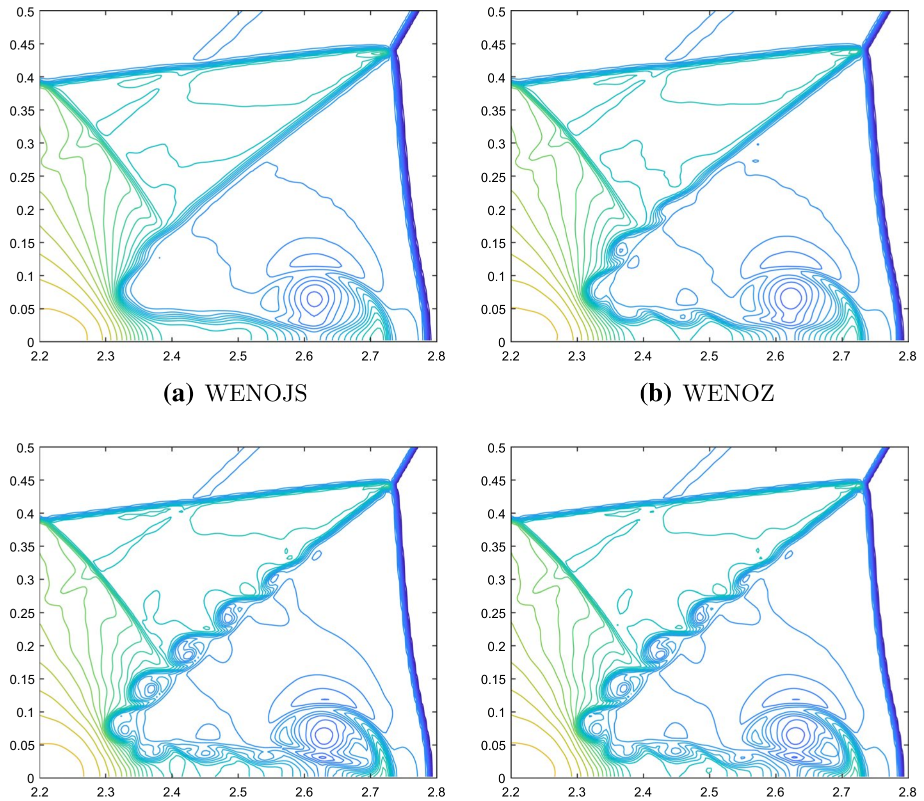

(a) WENOJS **(b)** WENOZ

(c) WENOJS-H **(d)** WENOZ-H

Fig. 35 Zoom-in figures for the double Mach reflection problem. Uniform mesh with 960×240 cells at time $T = 0.2$. Forty-three equally spaced density contours from 1.887 to 22.9

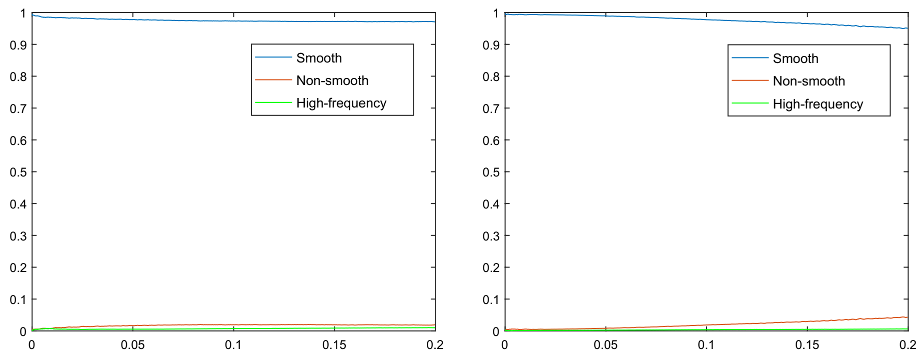

(a) x direction **(b)** y direction

Fig. 36 Double Mach reflection problem: history of ratios of different routes usage for WENOZ-H. Left: usage for x-direction; right: usage for y-direction

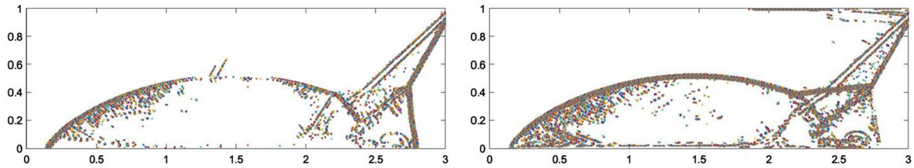

(a) Ratio of $flag_x$: 2.79% **(b)** Ratio of $flag_y$: 5.16%

Fig. 37 Double Mach reflection problem: distributions of $flag_x$ and $flag_y$ for the numerical solution computed by WENOZ-H at $T = 0.2$ checked by the hybrid indicator. Left: distribution of $flag_x$; right: distribution of $flag_y$

domain. The ratio of $flag_y$ is defined similarly. It shows that the simple hybrid indicator in the hybrid approach could capture the outline of discontinuities effectively.

Example 9 Rayleigh-Taylor instability problem [34]. The initial condition is

$$(\rho, u, v, P)^{\mathrm{T}} = \begin{cases} (2, 0, -0.025c\cos(8\pi x), 1 + 2y)^{\mathrm{T}}, y \in [0, 0.5), \\ (1, 0, -0.025c\cos(8\pi x), y + 1.5)^{\mathrm{T}}, y \in [0.5, 1], \end{cases} \tag{50}$$

where $c = \sqrt{\frac{\gamma P}{\rho}}$ is the sound speed with $\gamma = \frac{5}{3}$. We compute the numerical solution in the region $[0, 0.25] \times [0, 1]$. Reflective boundary conditions are imposed at the left and right sides of the domain. The bottom boundary condition is set as $(\rho, u, v, P) = (2, 0, 0, 1)$, while the top boundary condition is set as $(\rho, u, v, P) = (1, 0, 0, 2.5)$. The source term $g(x, y, t) = (0, 0, \rho, \rho v)^{\mathrm{T}}$ is added to the right-hand side of the Euler equations (48). We compute the numerical solution till $T = 1.95$. The numerical results for different schemes are shown in Fig. 38. Again, the hybrid schemes capture more details than the original ones. For the WENOZ-H scheme, the detection results in x- and y-directions at $T = 1.95$

Fig. 38 Numerical results of different WENO schemes for the Rayleigh-Taylor instability problem. Uniform mesh with 120×480 cells at time $T = 1.95$. Forty-three equally spaced density contours from 0.952 269 to 2.145 89. From left to right: WENOJS, WENOJS-H, WENOZ, and WENOZ-H

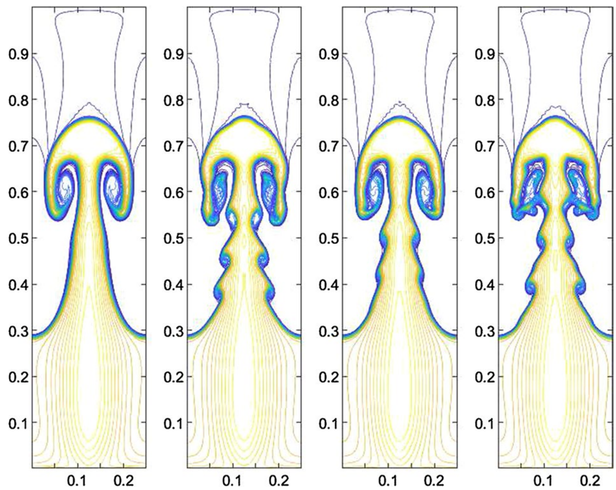

are shown in Fig. 39. We see that the indicator could capture the outline of discontinuities effectively.

Example 10 2D Riemann problem [22]. We compute the 2D Riemann problem in the region $[0, 1] \times [0, 1]$ with the initial condition

$$(\rho, u, v, P)^{\mathrm{T}} = \begin{cases} (1.5, 0, 0, 1.5)^{\mathrm{T}}, & x > 0.5, y > 0.5, \\ (0.532\,3, 1.206, 0, 0.3)^{\mathrm{T}}, & x < 0.5, y > 0.5, \\ (0.138, 1.206, 1.206, 0.029)^{\mathrm{T}}, & x < 0.5, y < 0.5, \\ (0.532\,3, 0, 1.206, 0.3)^{\mathrm{T}}, & x > 0.5, y < 0.5. \end{cases} \tag{51}$$

The final computational time is $T = 0.3$. The numerical results for different schemes are shown in Fig. 40, and the zoomed-in figure is shown in Fig. 41. We can see that the hybrid WENO schemes capture more accurate details in flow field than the original schemes. The detection results in the WENOZ-H scheme at $T = 0.3$ are shown in Fig. 42, which gives an effective capture of the outline of discontinuities.

Example 11 The 2D implosion problem [26]. The initial condition is given by

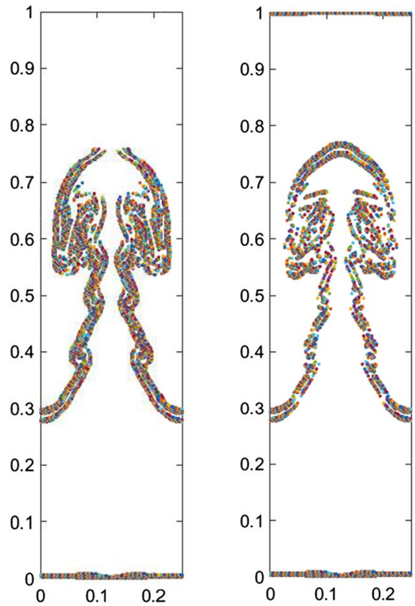

(a) Ratio of $flag_x$: 8.02% **(b)** Ratio of $flag_y$: 6.33%

Fig. 39 Rayleigh-Taylor instability problem: distributions of $flag_x$ and $flag_y$ for the numerical solution computed by WENOZ-H at $T = 1.95$ checked by the hybrid indicator. Left: distribution of $flag_x$; right: distribution of $flag_y$

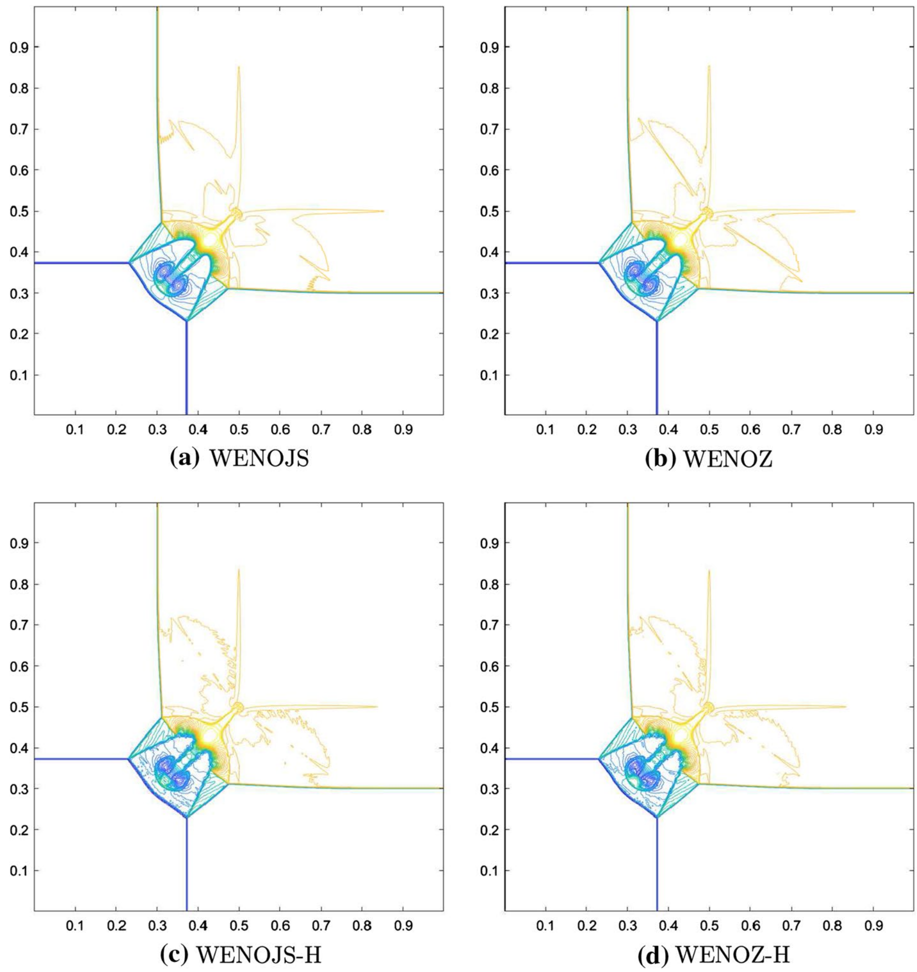

Fig. 40 Numerical results for the 2D Riemann problem. Uniform mesh with $1\,024 \times 1\,024$ cells at time $T = 0.3$. Forty-three equally spaced density contours from 0.14 to 1.7

$$(\rho, u, v, P)^{\mathrm{T}} = \begin{cases} (0.125, 0, 0, 0.14)^{\mathrm{T}}, 0.15 < x < 0.45, 0.15 < y < 0.45, \\ (1, 0, 0, 0.1)^{\mathrm{T}}, \qquad\qquad \text{otherwise}. \end{cases} \tag{52}$$

The computational domain is a square with size 0.6 with the periodic boundary condition. We compute the solution till $T = 0.75$, and the numerical results are shown in Fig. 43. The schemes after hybridization perform very similarly and increase the resolution on flow details. For the WENOZ-H scheme, the detection results in x- and y-directions at $T = 0.75$ are shown in Fig. 44. We can still see that the indicator could resolve the outline of discontinuities effectively.

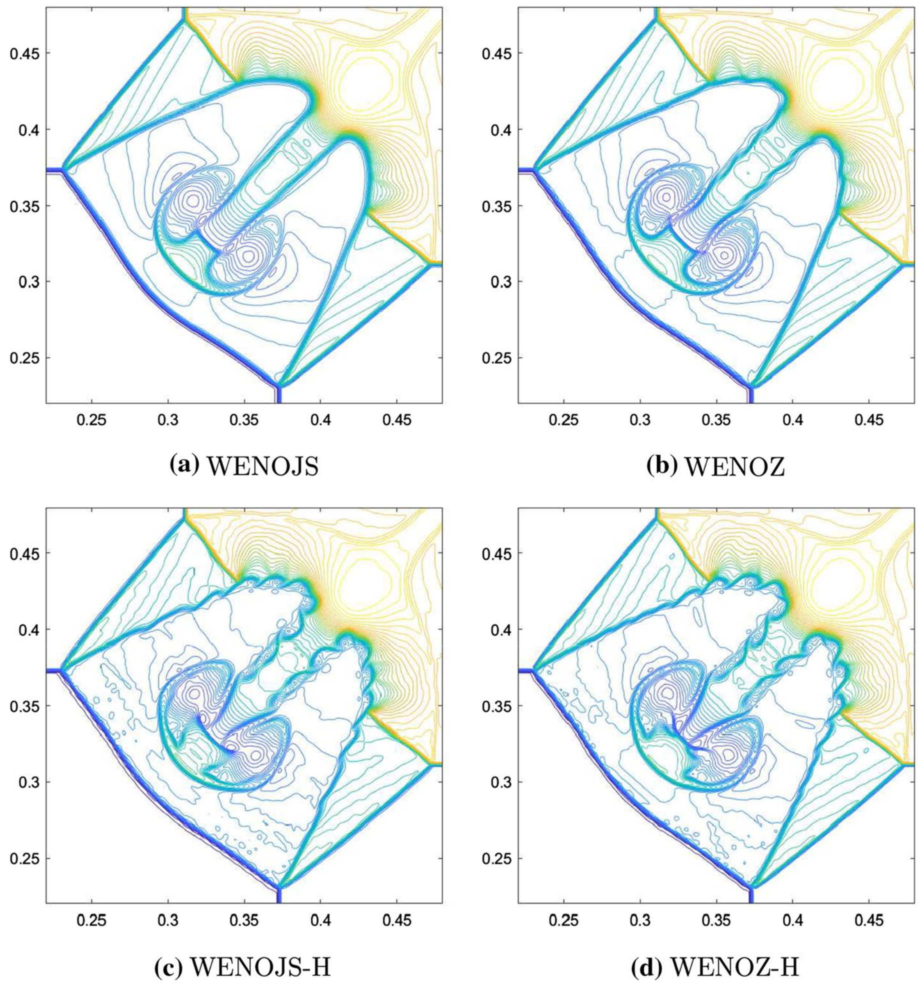

Fig. 41 Zoom-in figures for the 2D Riemann problem. Uniform mesh with $1\,024 \times 1\,024$ cells at time $T = 0.3$

Example 12 Next, we consider the forward step problem. The wind tunnel is 3 units length and 1 unit width. Initially, a Mach 3 flow with $(\rho, u, v, P)^{\mathrm{T}} = (1.4, 3.0, 0, 1.0)^{\mathrm{T}}$ goes from the left to the right. The step with height 0.2 units is located in the interval [0.6, 3]. Inflow and outflow boundary conditions are applied along the left and right boundaries, respectively, and reflective boundary conditions are imposed along the walls of the tunnel. Based on the assumption of a nearly steady flow, we adopt the method introduced in [41] to fix the singularity at the corner of the step. The numerical results are shown in Fig. 45. We can see that the hybrid schemes could resolve the slip line better than the classical schemes. For the WENOZ-H scheme, the detection results in x- and y-directions at $T = 4.0$ are shown in Fig. 46, where ratio of $flag_*$ is redefined as $\frac{\sum flag_*}{0.84 N_x N_y}$, since there is a step located at the lower part of whole computational domain. We can still see that the indicator could present a nice capture of discontinuities.

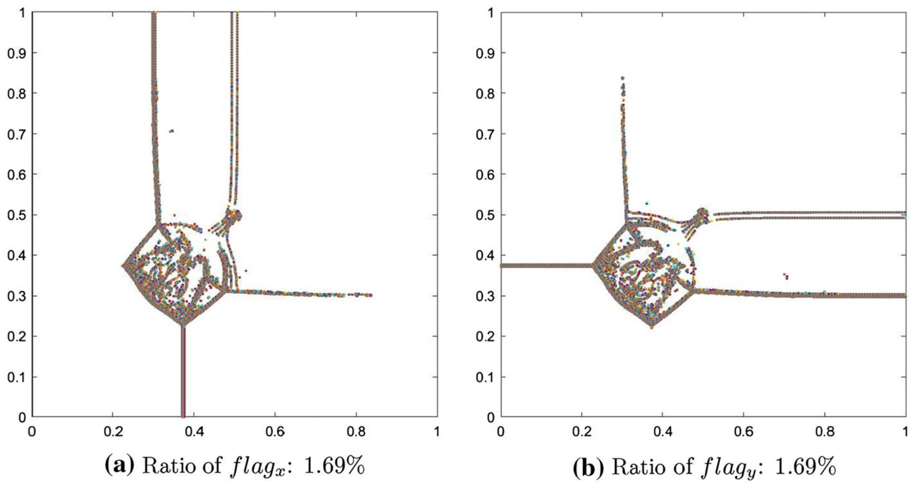

Fig. 42 2D Riemann problem: distributions of $flag_x$ and $flag_y$ for the numerical solution computed by WENOZ-H at $T = 0.3$ checked by the hybrid indicator. Left: distribution of $flag_x$; right: distribution of $flag_y$

At the end of this section, we present the CPU time for different problems computed by the classical schemes and the hybrid schemes in Table 1. For general hybrid schemes, the burdensome characteristic decomposition is removed in smooth region for efficiency. However, in our scheme, all the regions are classified based on the characteristic variables, and thus, the computational cost is not significantly reduced.

5 Conclusion

In this paper, a new kind of hybrid approach was proposed for the WENO-type reconstruction. Different from the existing hybrid methods, the reconstruction stencil is identified as smooth, non-smooth, and high-frequency regions by adopting the linear, WENO, and mixed reconstruction, respectively. The motivation is to increase the spectral resolution, which has been verified by the approximate spectral analysis and numerous numerical examples. The corresponding hybrid WENO finite difference schemes were proposed based on two classical WENO schemes for hyperbolic conservation laws, respectively. In numerical experiments, the hybrid schemes could achieve more accurate performance than the original schemes in the smooth region, better resolution in complex fluid field, and maintain the sharp and oscillation-free resolution near shocks. The new features of these hybrid WENO schemes are their simplicity and flexibility. No matter which original WENO scheme is used, the hybrid schemes perform very similarly. This hybrid approach can be applied to the finite volume method easily and will be generalized to higher order reconstruction.

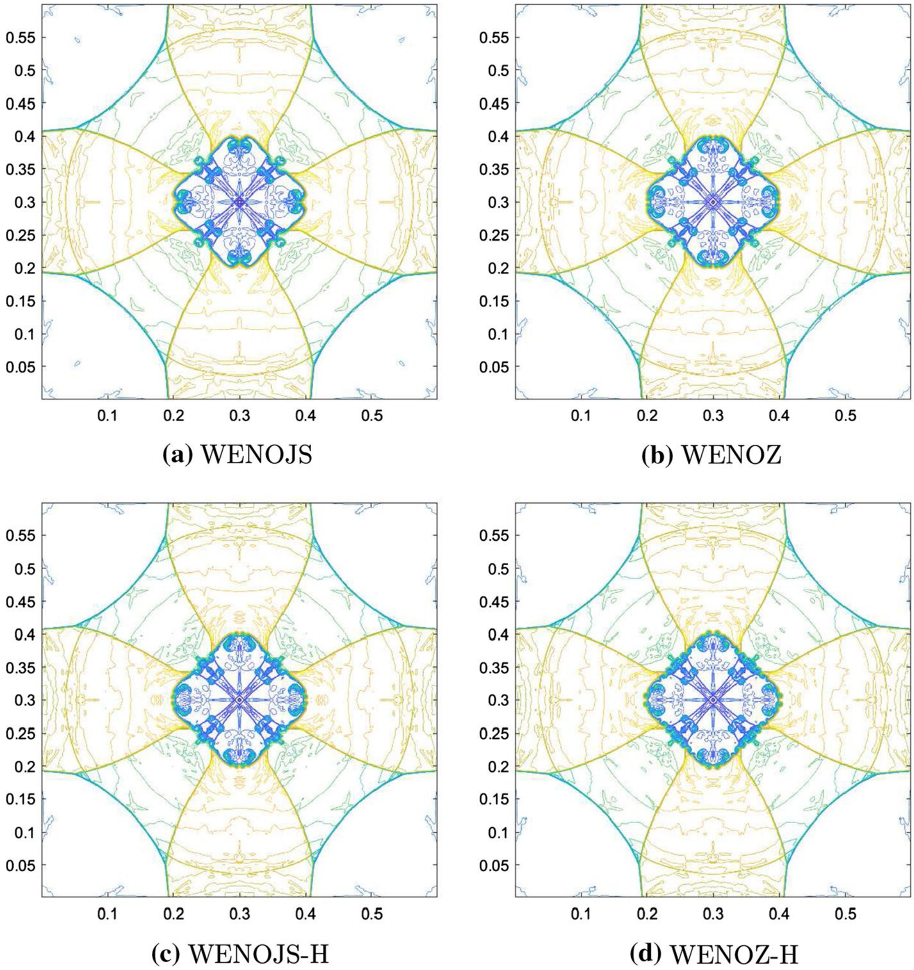

Fig. 43 Numerical results for the 2D implosion problem. Uniform mesh with $1\,024 \times 1\,024$ cells at time $T = 0.75$. Forty-three equally spaced density contours from 0.3 to 1.2

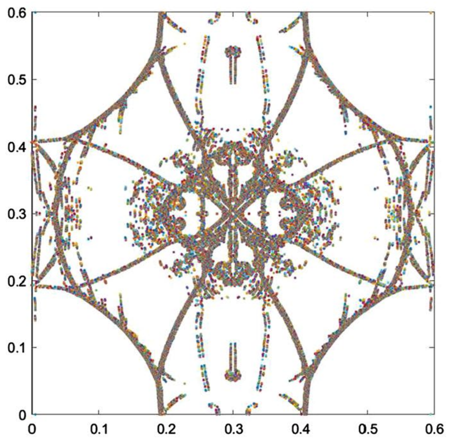

(a) Ratio of $flag_x$: 5.69% **(b)** Ratio of $flag_y$: 5.69%

Fig. 44 2D implosion problem: distributions of $flag_x$ and $flag_y$ for the numerical solution computed by WENOZ-H at $T = 0.75$ checked by the hybrid indicator. Left: distribution of $flag_x$; right: distribution of $flag_y$

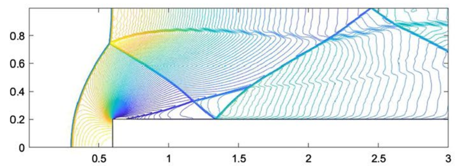

(a) WENOJS **(b)** WENOZ

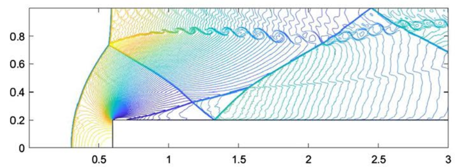

(c) WENOJS-H **(d)** WENOZ-H

Fig. 45 Numerical results for the forward step problem. Uniform mesh with 900×300 cells at time $T = 4.0$. Ninety equally spaced density contours from 0.32 to 6.15

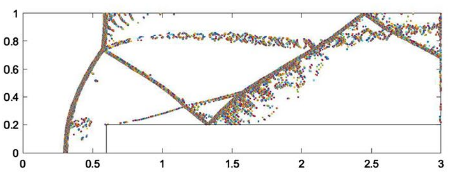

(a) Ratio of $flag_x$: 4.21% **(b)** Ratio of $flag_y$: 6.78%

Fig. 46 Forward step problem: distributions of $flag_x$ and $flag_y$ for the numerical solution computed by WENOZ-H at $T = 4.0$ checked by the hybrid indicator. Left: distribution of $flag_x$; Right: distribution of $flag_y$

Table 1 CPU time(s) for different problems computed by the classical schemes and the hybrid schemes

Problem	WENOJS	WENOJS-H	WENOZ	WENOZ-H
Lax	39.01	36.00	38.54	35.86
Sod	22.98	20.75	22.71	21.14
Shu-Osher	19.66	17.80	19.57	18.17
Blast	35.88	32.77	35.72	33.38
Sedov	53.28	55.65	56.59	54.15
DM	4 654	4 524	4 780	4 513
RT	2 642	2 464	2 630	2 492
RI	13 967	12 545	14 228	12 575
IM	58 262	56 343	60 025	56 300

Lax: Lax's problem with mesh size 3 000. Sod: Sod's problem with mesh size 3 000. Shu-Osher: the shock density wave interaction problem with mesh size 2 000. Blast: the interaction of two blast waves problem with mesh size 2 000. Sedov: the Sedov's blast wave problem with mesh size 2 000. DM: double Mach reflection problem with mesh size 960×240. RT: Rayleigh-Taylor instability problem with mesh size 120×480. RI: 2D Riemann problem with mesh size $1\,024 \times 1\,024$. IM: 2D implosion problem with mesh size $1\,024 \times 1\,024$

Compliance with Ethical Standards

Conflict of Interest On behalf of all authors, the corresponding author states that there is no conflict of interest.

References

1. Acker, F., de R. Borges, R.B., Costa, B.: An improved WENO-Z scheme. J. Comput. Phys. **313**, 726–753 (2016)
2. Adams, N.A., Shariff, K.: A high-resolution hybrid compact-ENO scheme for shock-turbulence interaction problems. J. Comput. Phys. **127**(1), 27–51 (1996)
3. Baeza, A., Burger, R., Mulet, P., Zorio, D.: On the efficient computation of smoothness indicators for a class of WENO reconstructions. J. Sci. Comput. **80**(2), 1240–1263 (2019)
4. Bhise, A.A., Samala, R.: An efficient hybrid WENO scheme with a problem independent discontinuity locator. Int. J. Numer. Methods Fluids **91**(1), 1–28 (2019)
5. Borges, R., Carmona, M., Costa, B., Don, W.-S.: An improved weighted essentially non-oscillatory scheme for hyperbolic conservation laws. J. Comput. Phys. **227**(6), 3191–3211 (2008)
6. Castro, M., Costa, B., Don, W.-S.: High order weighted essentially non-oscillatory WENO-Z schemes for hyperbolic conservation laws. J. Comput. Phys. **230**(5), 1766–1792 (2011)
7. Cockburn, B., Shu, C.-W.: TVB Runge-Kutta local projection discontinuous Galerkin finite element method for conservation laws. II. General framework. Math. Comput. **52**(186), 411–435 (1989)
8. Costa, B., Don, W.-S.: Multi-domain hybrid spectral-WENO methods for hyperbolic conservation laws. J. Comput. Phys. **224**(2), 970–991 (2007)
9. Don, W.-S., Gao, Z., Li, P., Wen, X.: Hybrid compact-WENO finite difference scheme with conjugate Fourier shock detection algorithm for hyperbolic conservation laws. SIAM J. Sci. Comput. **38**(2), A691–A711 (2016)
10. Fan, P., Shen, Y., Tian, B., Yang, C.: A new smoothness indicator for improving the weighted essentially non-oscillatory scheme. J. Comput. Phys. **269**, 329–354 (2014)
11. Fidalgo, J.F., Nogueira, X., Ramirez, L., Colominas, I.: An a posteriori, efficient, high-spectral resolution hybrid finite-difference method for compressible flows. Comput. Methods Appl. Mech. Eng. **335**, 91–127 (2018)

12. Fu, L.: A hybrid method with TENO based discontinuity indicator for hyperbolic conservation laws. Commun. Comput. Phys. **26**(4), 973–1007 (2019)
13. Fu, L., Hu, X.Y., Adams, N.A.: A family of high-order targeted ENO schemes for compressible-fluid simulations. J. Comput. Phys. **305**, 333–359 (2016)
14. Gottlieb, S., Shu, C.-W., Tadmor, E.: Strong stability-preserving high-order time discretization methods. SIAM Rev. **43**, 89–112 (2001)
15. Ha, Y., Kim, C.H., Lee, Y.J., Yoon, J.: An improved weighted essentially non-oscillatory scheme with a new smoothness indicator. J. Comput. Phys. **232**(1), 68–86 (2013)
16. Harten, A.: Adaptive multiresolution schemes for shock computations. J. Comput. Phys. **115**(2), 319–338 (1994)
17. Harten, A., Engquist, B., Osher, S., Chakravarthy, S.R.: Uniformly high order accurate essentially non-oscillatory schemes, iii. J. Comput. Phys. **131**(1), 3–47 (1987)
18. Henrick, A.K., Aslam, T.D., Powers, J.M.: Mapped weighted essentially non-oscillatory schemes: achieving optimal order near critical points. J. Comput. Phys. **207**(2), 542–567 (2005)
19. Jiang, G.-S., Shu, C.-W.: Efficient implementation of weighted ENO schemes. J. Comput. Phys. **126**(1), 202–228 (1996)
20. Kim, C.H., Ha, Y., Yoon, J.: Modified non-linear weights for fifth-order weighted essentially non-oscillatory schemes. J. Sci. Comput. **67**(1), 299–323 (2016)
21. Krivodonova, L., Xin, J., Remacle, J.-F., Chevaugeon, N., Flaherty, J.E.: Shock detection and limiting with discontinuous Galerkin methods for hyperbolic conservation laws. Appl. Numer. Math. **48**(3/4), 323–338 (2004)
22. Lax, P.D., Liu, X.-D.: Solution of two-dimensional Riemann problems of gas dynamics by positive schemes. SIAM J. Sci. Comput. **19**(2), 319–340 (1998)
23. Li, G., Lu, C., Qiu, J.: Hybrid well-balanced WENO schemes with different indicators for shallow water equations. J. Sci. Comput. **51**, 527–559 (2012)
24. Li, G., Qiu, J.: Hybrid weighted essentially non-oscillatory schemes with different indicators. J. Comput. Phys. **229**, 8105–8129 (2010)
25. Li, G., Qiu, J.: Hybrid WENO schemes with different indicators on curvilinear grid. Adv. Comput. Math. **40**, 747–772 (2014)
26. Liska, R., Wendroff, B.: Comparison of several difference schemes on 1D and 2D test problems for the Euler equations. SIAM J. Sci. Comput. **25**(3), 995–1017 (2003)
27. Liu, X.-D., Osher, S., Chan, T.: Weighted essentially non-oscillatory schemes. J. Comput. Phys. **115**(1), 200–212 (1994)
28. Luo, X., Wu, S.-P.: Improvement of the WENO-Z+ scheme. Comput. Fluids **218**, 104855 (2021)
29. Pirozzoli, S.: Conservative hybrid compact-WENO schemes for shock-turbulence interaction. J. Comput. Phys. **178**(1), 81–117 (2002)
30. Pirozzoli, S.: On the spectral properties of shock-capturing schemes. J. Comput. Phys. **219**(2), 489–497 (2006)
31. Qiu, J., Shu, C.-W.: A comparison of troubled-cell indicators for Runge-Kutta discontinuous Galerkin methods using weighted essentially nonoscillatory limiters. SIAM J. Sci. Comput. **27**(3), 995–1013 (2005)
32. Ren, Y.-X., Liu, M., Zhang, H.: A characteristic-wise hybrid compact-WENO scheme for solving hyperbolic conservation laws. J. Comput. Phys. **192**(2), 365–386 (2003)
33. Sedov, L.I., Friedman, M., Street, R.E.: Similarity and dimensional methods in mechanics. Phys. Today **13**(9), 50–52 (2009)
34. Shi, J., Zhang, Y.-T., Shu, C.-W.: Resolution of high order WENO schemes for complicated flow structures. J. Comput. Phys. **186**(2), 690–696 (2003)
35. Shu, C.-W.: High order weighted essentially nonoscillatory schemes for convection dominated problems. SIAM Rev. **51**(1), 82–126 (2009)
36. Shu, C.-W., Osher, S.: Efficient implementation of essentially non-oscillatory shock-capturing schemes, II. J. Comput. Phys. **83**(1), 32–78 (1989)
37. Sun, Z., Wang, S., Chang, L.-B., Xing, Y., Xiu, D.: Convolution neural network shock detector for numerical solution of conservation laws. Commun. Comput. Phys. **28**(5), 2075–2108 (2020)
38. Suresh, A., Huynth, H.: Accurate monotonicity-preserving schemes with Runge-Kutta time stepping. J. Comput. Phys. **136**(1), 83–99 (1997)
39. Wang, B.S., Don, W.-S., Gao, Z., Wang, Y.H., Wen, X.: Hybrid compact-WENO finite difference scheme with radial basis function based shock detection method for hyperbolic conservation laws. SIAM J. Sci. Comput. **40**(6), A3699–A3714 (2018)
40. Wen, X., Don, W.-S., Gao, Z., Hesthaven, J.S.: An edge detector based on artificial neural network with application to hybrid Compact-WENO finite difference scheme. J. Sci. Comput. **83**, 49 (2020)

41. Woodward, P., Colella, P.: The numerical simulation of two-dimensional fluid flow with strong shocks. J. Comput. Phys. **54**(1), 115–173 (1984)
42. Yamaleev, N.K., Carpenter, M.H.: A systematic methodology for constructing high-order energy stable WENO schemes. J. Comput. Phys. **228**(11), 4248–4272 (2009)
43. Yamaleev, N.K., Carpenter, M.H.: Third-order energy stable WENO scheme. J. Comput. Phys. **228**(8), 3025–3047 (2009)
44. Zhang, S., Zhu, J., Shu, C.-W.: A brief review on the convergence to steady state solutions of Euler equations with high-order WENO schemes. Adv. Aerodyn. **1**(1), 1–25 (2019)
45. Zhao, Z., Chen, Y., Qiu, J.: A hybrid Hermite WENO scheme for hyperbolic conservation laws. J. Comput. Phys. **405**, 109175 (2020)
46. Zhao, Z., Zhu, J., Chen, Y., Qiu, J.: A new hybrid WENO scheme for hyperbolic conservation laws. Comput. Fluids **179**, 422–436 (2019)
47. Zhu, H., Qiu, J.: Adaptive Runge-Kutta discontinuous Galerkin methods using different indicators: one-dimensional case. J. Comput. Phys. **228**(18), 6957–6976 (2009)
48. Zhu, J., Qiu, J.: A new fifth order finite difference WENO scheme for solving hyperbolic conservation laws. J. Comput. Phys. **318**, 110–121 (2016)
49. Zhu, J., Shu, C.-W.: A new type of multi-resolution WENO schemes with increasingly higher order of accuracy. J. Comput. Phys. **375**, 659–683 (2018)